2011

Fracture Toughness of NUCu-140 Simulated Heat Affected Zones

Brett Leister
Lehigh University

Fracture Toughness of NUCu-140 Simulated Heat Affected Zones

by

Brett Leister

A Thesis

Presented to the Graduate and Research Committee

of Lehigh University

in Candidacy for the Degree of

Master of Science

In

Mechanical Engineering

Lehigh University

May 2011

This thesis is accepted and approved in partial fulfillment of the requirements for the Master of Science.

_____

Date

_____

Dr. John N. DuPont, Thesis Advisor

_____

Dr. D. Gary Harlow, Chairperson of Department

Table of Contents

List of Tables iv

List of Figures v

Acknowledgements vii

Abstract 1

1. Introduction 2

1.1 NUCu-140 Base Material 2

1.2 K Fracture Toughness Background 2

1.2.1 K Fracture Toughness Assumptions 3

1.3 Introduction to the J-Integral 4

1.3.1 Unloading Compliance Testing Method 5

1.3.2 J_{IC} Failure Criterion 6

1.4 Changes in J-Integral Values 7

1.5 Plastic Zone Size and J-Integral Changes During Testing 10

1.5.1 Sample Geometry Influences 10

1.5.2 Sample Thickness Influences 11

1.5.3 Crack Length Influences 12

1.6 Fracture Toughness of Copper Precipitation Strengthened Steels 14

1.6.1 Dislocation Motion Effects on Fracture Toughness 15

1.6.2 Effect of Copper Additions 16

1.6.3 Fracture Toughness of Thermally Simulated Heat Affected Zones 21

1.7 Role of Second Phase Particles on Fracture Toughness 23

1.7.1 Influence of Stress Triaxiality 24

1.7.2 Influence of Manganese Sulfide (MnS) Inclusions 26

1.7.3. Particle Size Effects on Fracture Toughness 27

1.7.4 Influence of Carbides 28

1.7.5 Influence of Second-Phase Microstructure 29

1.8 Experimental Objective 33

2. Experimental Procedure 34

3. Results and Discussion 36

3.1 Microstructure of Gleeble Thermal Simulations 36

3.2 Grain Size of Simulated HAZ Samples 38

3.3 Microhardness of Simulated HAZ Samples 39
3.4 Fracture Toughness of Simulated HAZ Samples 39
3.5 Fractography of Simulated HAZ Samples 41
3.6 EDS Analysis of Particles at Microvoids 44
3.7 MatCalc Results 46
3.8 Discussion 47
4. Conclusions 51
5. References 52
6. Vita 54

List of Tables

Table 1: Calculated J-integrals at various cycles of crack extension[16] 14
Table 2: Chemical composition of NUCu-140 (all values in wt%). 34

List of Figures

Figure 1: Plastic zone sizes during fracture toughness testing in plane stress and plane strain conditions[5] 4
Figure 2: Example of line contour used for calculation of J-integral 5
Figure 3: Schematic showing the relation between integration contour and radius of the plastic zone[10] 7
Figure 4: (a) Comparison of plastic zone to J-integral contours, (b) Normalized J-integral values versus normalization of contour radius[10] 8
Figure 5: Elastic plastic boundary (plastic zone size) in SENB bar for increasing J integral values[11] 9
Figure 6: Schematic showing increasing plastic zone size with increasing load in SENB[12] 9
Figure 7: Slip line fields for three different sample configurations[9] 10
Figure 8: Variation of J fracture toughness with specimen thickness[14] 11
Figure 9: Influence of a/W ratio on J fracture toughness for HSLA steels[15] 12
Figure 10: Plastic zones computed during three loading and unloading cycles undergoing fracture toughness finite element calculations[16] 13
Figure 11: Fracture toughness as a function of strength level for HSLA-100 steels with varying copper content. The numbers on the plot indicate the ageing temperatures in °C following water quenching.[19] 16
Figure 12: Fracture toughness as a function of carbon equivalent within stable austenite phases compared to data seen for a variety of steels.[19] 17
Figure 13: Relationship between hardness change (before and after tempering) to the cooling time (T8-5)[20] 18
Figure 14: SEM micrographs showing the influence of processing conditions on the microstructure of HSLA-100 (a) water quenched (WQ), (b) WQ and aged at 400°C, (c) WQ and aged at 500°C, (d) WQ and aged at 600°C, (e) WQ and aged at 650°C, (f) WQ and aged at 700°C[21] 19
Figure 15: (a) JR Curves for differing ageing temperatures in HSLA-100 steel, (b) Fracture toughness as a function of ageing temperature in HSLA-100 steel[21] 20
Figure 16: Effect of cooling time on the fracture toughness in the (a) T-L orientation and (b) L-T orientation[22] 21
Figure 17: Effect of peak temperature on the fracture toughness in the (a) T-L orientation and (b) L-T orientation[22] 22
Figure 18: Growth and link up of microvoids to form a ductile crack in a free-cutting mild steel.[3] 24
Figure 19: SEM micrographs of the fracture surfaces the coarse grained HAZ of HY-100 with stress triaxiality increasing from A to C.[25] 25
Figure 20: SEM micrographs showing the various morphologies of MnS inclusions (a) Type I (b) Type II (c) Type III[3] 26
Figure 21: Relationship between initiation fracture toughness and the size of the initiation site.[28] 28

Figure 22: Effect of second phase particles on the ductility of steel[3] 29
Figure 23: Plastic deformation within neighboring bands of granular ferrite and equiaxed ferrite in HY-100 steel[26] 30
Figure 24: Microstructure of HSLA steel showing increasing amounts of blocky MA constituent at the grain boundaries after intercritical heating on the second pass to (a) 764°C (b) 778°C (c) 785°C and (d) 804°C[27] 31
Figure 25: Impact energy as a function of temperature showing low toughness in the intercritically heated region[27] 31
Figure 26: Cross section of charpy fracture surface in which the failure runs along the prior austenite grain boundaries after originating at debonded MA constituent (dark spot in A).[27] 32
Figure 27: Impact energy as a function of temperature for various cooling times after the second weld pass[27] 33
Figure 28: Dimension of fracture toughness bar used for testing. All dimensions are in mm, and the sample is 8mm thick. 35
Figure 29: Light optical micrographs of NUCu-140 showing an equiaxed ferrite microstructure for peak temperatures of (a) base metal, (b) 675°C, (c) 800°C, and (d) 900°C. (e) The 1350°C peak temperature microstructure consists of acicular ferrite, bainite, and martensite. Etched with 3% nital. 37
Figure 30: Grain size measurements for NUCu-140 HAZ thermal simulations. 38
Figure 31: Vickers microhardness of NUCu-140 HAZ thermal simulations. 39
Figure 32: Crack growth resistance curves (J-R curves) for NUCu-140 thermal simulations. 40
Figure 33: Average fracture toughness values (J_Q) of NUCu-140 thermal simulations showing a maximum at the 900°C peak temperature. 41
Figure 34: Low magnification SEM images of fracture surfaces for (a) NUCu-140 base metal, and thermal simulations with peak temperatures of (b) 675°C, (c) 800°C, (d) 900°C, and (e) 1350°C. Note that the fracture surface above the white line was induced following testing. 42
Figure 35: Fracture surfaces of NUCu-140 thermal simulations showing ductile failure via microvoid coalescence for peak temperatures of (a) base metal, (b) 675°C, (c) 800°C, and (d) 900°C. Areas of cleavage fracture are seen in (e) the 1350°C peak temperature specimen. 43
Figure 36: SEM micrographs and EDS spectra showing (a) line of microcracks ahead of a ridge in base metal sample, (b-c) particle at the edge of a microcrack shown to be an aluminum rich particle. 45
Figure 37: SEM micrographs and EDS spectra showing (a) line of microcracks ahead of a ridge in 900°C peak temperature sample, (b-c) particle at the edge of a microcrack shown to be an aluminum rich particle. 46
Figure 38: LEAP tomography data from NUCu-140 showing radius, number density, and phase fraction of copper precipitates in the base metal, heat affected zone, and fusion zone.[1] 48
Figure 39: Close-up view of crack tip blunting region of NUCu-140 JR curves 50

Acknowledgements

I would like to thank parents and my brother for the advice they have given and sacrifices they have made over the years to put me in the position I am today. Thank you to Prof. DuPont for your guidance throughout all of the research for this project. Keith Donald has been an invaluable resource when I needed to talk about testing methods and data interpretation. Without him, I would not have been able to complete my research. Thank you to Mike Rex and John Gregoris for machining countless numbers of samples that were only going to be broken. Thank you to Sam Lawrence and Arlan Benscoter for all of their assistance and metallurgical wisdom. Thanks to the Engineering Metallurgy Group, past and present, Ken Adams, Jeff Farren, Andrew Stockdale, Greg Brentrup, and Dan Bechetti for listening to my endless hours of complaints and for helping me with whatever was needed to get our projects done. Thank you to all of my friends for keeping me sane throughout these last few years.

Abstract

NUCu-140 is a copper-precipitation strengthened steel that is a candidate material for many new structural applications, including naval ship hulls. It has a simple chemistry and is manufactured using basic techniques. Before this new alloy can be fully utilized, its mechanical behavior following welding must be determined. Previous research has been conducted by Farren et. al.[1] to correlate the microstructure and evolution of copper precipitates in the heat affected zone (HAZ) to the mechanical behavior seen in those locations. This research builds on that previous work by extending the study to include fracture toughness and fractography of the base metal along with the four major regions of the HAZ. Microhardness and grain size measurements were also performed. Results show that a reduction in hardness, increase in fracture toughness, and failure mode of microvoid coalescence is seen from the base metal up to and including the fully recrystallized HAZ, followed by an increase in hardness, decrease in fracture toughness, and regions of cleavage failure in the coarse grained HAZ (CGHAZ). These observations are primarily a result of the evolution of the copper precipitates in those regions, with a contribution from the overall microstructure. Grain size does not change significantly, except in the CGHAZ where a 6 fold increase was seen.

1. Introduction

1.1 NUCu-140 Base Material

NUCu-140 is a type of high strength low carbon (HSLC) steel that shows promise as a new candidate material for fabrication of naval ship hulls. This alloy shows a reduction in cost in three ways. First, expensive alloying elements, such as chromium, have been minimized or eliminated. Second, it is manufactured using simple and inexpensive processing methods, and third, its increased strength and toughness allows for structural designs which use less of the material. Elimination of chromium is also beneficial for protection of welders due to the removal of the carcinogenic hexavalent chromium from the welding fume. During arc welding of precipitation strengthened materials, a locally softened region can form within the heat affected zone (HAZ), which is a result of a change in the morphology of the precipitates in that region.[2] The various regions of the heat-affected zone, the sub-critical region, inter-critical region, fully recrystallized region, and the coarse-grained HAZ[3], are expected to exhibit different properties based upon the differing thermal cycles experienced throughout the material.

1.2 K Fracture Toughness Background

Typically, tensile testing is the method chosen to get baseline information about varying properties within a material. This may not be the best, or most informative, test to perform because tensile testing assumes a perfect material (i.e. no cracks, voids, etc.), but this is very rarely the case for an engineering material. Instead, fracture toughness is chosen in order to correlate the largest defect present in the material to an applied stress in order to determine a stress intensity factor, K, given by Equation 1.

Equation 1: Stress Intensity Factor

$$K = \sigma\sqrt{\pi a}$$

where σ is the applied stress, and a is the maximum defect size. The most common way to see a value reported is referred to as the plane-strain fracture toughness, K_{IC}, a worst case scenario in which the material would fail at the lowest possible K value.

1.2.1 K Fracture Toughness Assumptions

K fracture toughness is not the most ideal fracture toughness parameter because of the assumptions it required for calculations, most notably, the criteria of small-scale yielding. For use of linear-elastic fracture mechanics (K fracture toughness) as a one parameter failure criterion, Begley and Landes stated that the plastic region at the crack tip must be at least one order of magnitude smaller than the physical dimensions of the sample being tested.[4] Hutchinson extended this criterion even further to say that the uncracked ligament and the crack itself must be greater than $25r_p$, where r_p is the radius of the plastic zone, once failure has occurred. The plastic zone size is altered depending on whether plane stress or plane strain conditions are seen, and the equations and contour describing the two can be seen in Equation 2 and Figure 1, respectively.[5]

Equation 2: Radius of the plastic zone during fracture toughness testing

$$r_p = \left(\frac{1}{3\pi}\right)\left(\frac{K}{\sigma_o}\right)^2 \quad for\ plane\ strain$$

$$r_p = \left(\frac{1}{\pi}\right)\left(\frac{K}{\sigma_o}\right)^2 \quad for\ plane\ stress$$

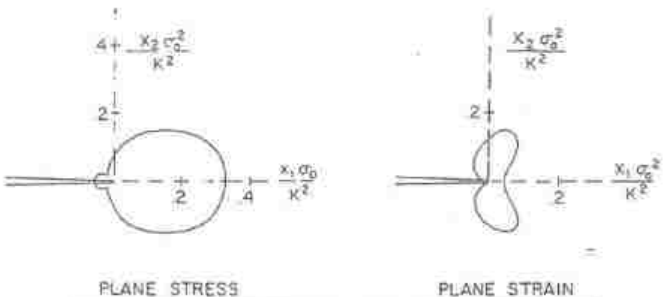

Figure 1: Plastic zone sizes during fracture toughness testing in plane stress and plane strain conditions[5]

The requirements described by Hutchinson require that for plane strain conditions to exist, which have a plastic zone size 1/3 that of plane stress conditions, and a sample with a plastic zone of 10mm such as for an intermediate-strength steel, the sample would have to be over 250mm thick. This makes testing on a lab scale nearly impossible.

1.3 Introduction to the J-Integral

The J-integral was developed as a way to try to account for the problem of large plastic zone sizes at the crack tip in highly ductile samples. The idea was first proposed by Rice as a way to determine the fracture toughness of a sample that displayed such characteristics.[6] The significance of the J-integral is that the crack tip area can be characterized without focusing attention directly at the tip itself, but by analyzing a path integral around, and including, the crack tip. An example of the path integral can be seen in Figure 2 and Equation 3,

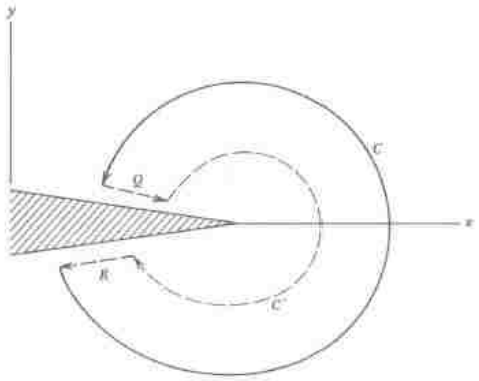

Figure 2: Example of line contour used for calculation of J-integral[7]

Equation 3: J-integral

$$J = \oint W\, dy - T\, \frac{\partial u}{\partial x}\, ds$$

where x and y are coordinates normal to the crack front, ds is an increment along the contour, T is a stress vector acting along the contour, u is the displacement vector, and W is the strain energy density. In order for this integral to be a viable solution for characterizing the behavior at the crack tip, path independence of the contour must be maintained, as explained by Hertzberg.[7] Rice also states that the J-integral can be thought of as the change in potential energy of the material as a crack is propagated.[6]

1.3.1 Unloading Compliance Testing Method

Originally, J fracture toughness tests were conducted in such a way that one sample was used for one test only, but the work of Clarke et al. has shown that one sample can be used for conducting multiple tests.[8] This was achieved by repeatedly loading and unloading the material

in order to determine the J fracture toughness according to the compliance change of the material. However, unloading the material should not be allowed because it violates the deformation theory of plasticity. Although the deformation theory of plasticity is essentially a nonlinear elastic theory, it still does not allow for unloading due to the irreversibility of plastic deformation. Clarke et al. found that some unloading may be permitted due to the difference between the size of the plastic zone on unloading versus loading. Equation 4 shows the size of the plastic zone during unloading, which when compared to Equation 2 reveals that the plastic zone during unloading is 1/8 and 1/24 the size of the plastic zone during plane strain and plane stress loading, respectively.

Equation 4: Radius of the plastic zone during unloading portion of a J fracture toughness test

$$r_y = \left(\frac{1}{6\pi}\right)\left(\frac{K}{2\sigma_y}\right)^2$$

The final proof that small amounts of unloading are allowable came from the calculation of the parameter α, which is a ratio of the plastic zone size r_y (Equation 4) to process zone size Z_p, where $Z_p = J/\sigma_y$. In order for unloading to be allowed, $\alpha << 1$, with a suitable value being 0.01. Clarke et al. found that for 10% (from peak load) unloading resulted in $\alpha \approx 0.002$. This verification allows the J integral to be calculated multiple times from a single sample, saving time and money during testing.

1.3.2 J_{IC} Failure Criterion

It was desired to have a failure criterion similar to K_{IC} but using the J-integral, which is referred to as J_{IC}, where J_{IC} is the plane strain J fracture toughness. In order for J_{IC} to be a relevant single fracture toughness parameter, it needed to be independent of sample size and

geometry. The difficulty in this, however, is that when plastic behavior is present ahead of a crack tip, the geometry plays an integral part in the response of the sample. Plastic slip line theory shows that constraint, caused by changes in sample geometry, and/or loading conditions can cause changes in the flow fields ahead of the crack.[9]

1.4 Changes in J-Integral Values

In order for a constant J value to be determined, the contour of the integral must enclose the entire plastic zone around the crack tip, as well as the crack tip itself. If this is not satisfied, J will fluctuate within the plastic zone due to changes in potential energy. This was also shown by Kuang and Chen during their finite element studies on HY-130 steel.[10] The schematic in Figure 3 shows how the contour (r_1) cuts through the plastic zone. By varying the radius of the contour, Kuang and Chen were able to show that J only changes within the region of the plastic zone as seen in Figure 3 and Figure 4.

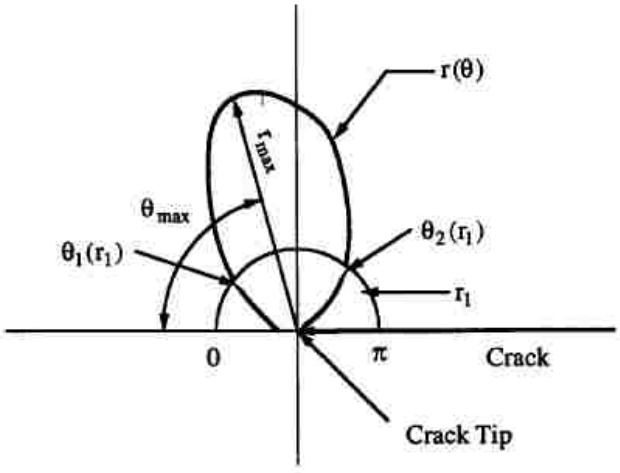

Figure 3: Schematic showing the relation between integration contour and radius of the plastic zone[10]

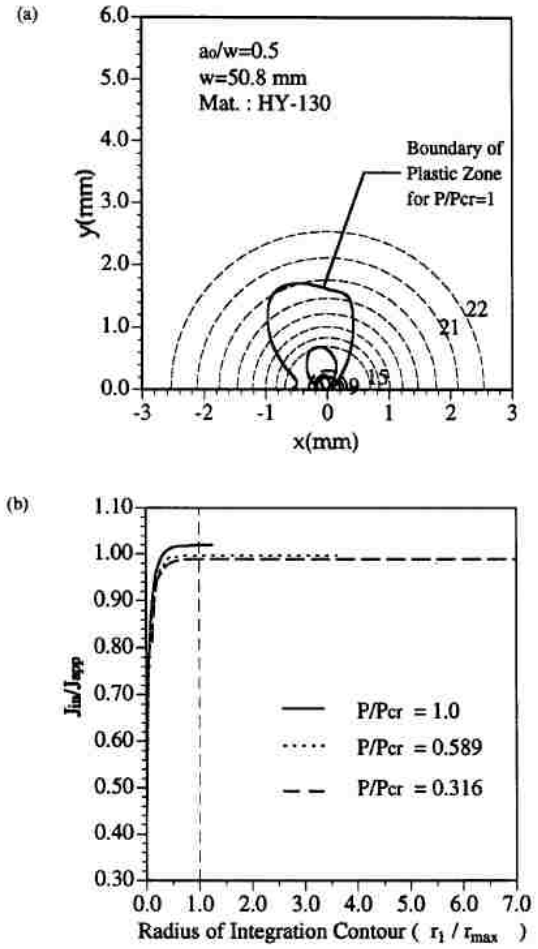

Figure 4: (a) Comparison of plastic zone to J-integral contours, (b) Normalized J-integral values versus normalization of contour radius[10]

It can be seen in Figure 4 that, the value of J is constantly changing when $r_1 < r_{max}$ and once $r_1 > r_{max}$ (signifying the integration contour completely surrounds the plastic zone) J remains constant.

Kudari et al.[11] have performed similar work, but have shown how the size of the plastic zone changes with increasing J. Figure 5 shows a single edge notched bend (SENB) bar that was used for finite element calculations.

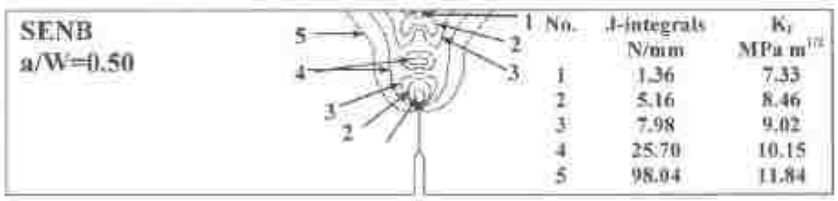

Figure 5: Elastic plastic boundary (plastic zone size) in SENB bar for increasing J integral values[11]

As the J-integral is increased, the size and shape of the plastic zone size contours change with it. When J is less than 5 the plastic zone was elliptical in nature, but as it is continually increased the zone takes on a bell shape. The shapes of the contours were controlled by the applied load as well as the neutral axis within the bend bar. There is a region of tensile stress and one of compressive stress, and when the edge of the compressive stress region meets with the plastic zone ahead of the crack tip, the compressive zone impedes the growth of the plastic zone.

Koko and Matthews[12] have shown the influence of increased loading on the size of the plastic zone in SENB specimens.

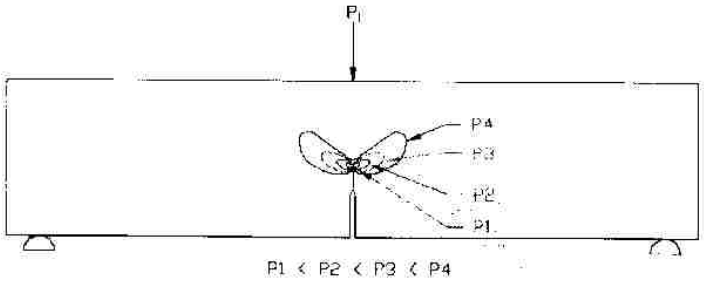

Figure 6: Schematic showing increasing plastic zone size with increasing load in SENB[12]

It is important to note the differences between the work of Kudari and Koko in order to fully understand the calculations. The calculations performed by Kudari et al. were done using plane

stress conditions, whereas the work by Koko and Matthews was done using plane strain conditions. This link is made even clearer when compared to the shape of the plastic zones proposed by Hutchinson (Figure 1).

1.5 Plastic Zone Size and J-Integral Changes During Testing

1.5.1 Sample Geometry Influences

Landes and Begley[9] performed the initial work to determine if a value, J_{IC}, could be determined that was independent of sample geometry and configuration, which is a difficult task considering the different types of specimens all yield in different ways, as shown by Figure 7.

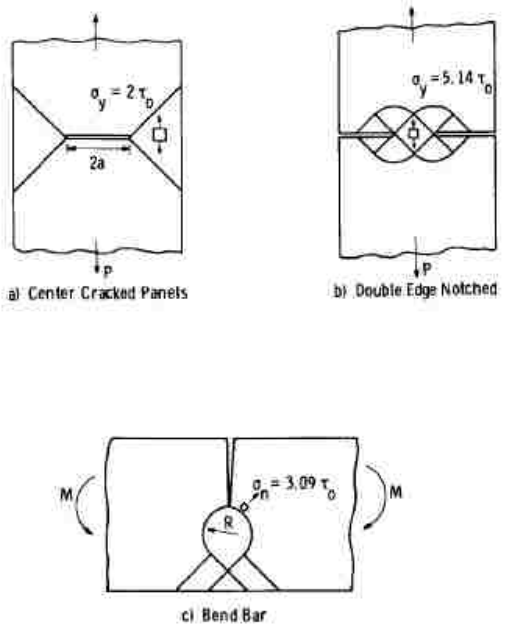

Figure 7: Slip line fields for three different sample configurations[9]

McClintock suggested that differences in hydrostatic stress (controlled by sample thickness) should alter the mode of crack extension in samples. Under conditions of high hydrostatic stress, initiation and growth of internal voids would be the controlling factor, and under conditions of low hydrostatic stress, slipping off on shear planes would take over.[13]

1.5.2 Sample Thickness Influences

When a sample is not thick enough, plane stress conditions prevail, and this leads to changes in the J-integral because it is only when plane strain conditions are reached that the fracture toughness value is constant, whether that is K_{IC} or J_{IC}. Typically, when a test specimen is thin in comparison to the other dimensions, plane stress conditions are applied. The work of Kulkarni et al.[14] proves this point. They performed J-fracture toughness tests on deep drawn sheet steel, with thickness less than 2mm. The results of J versus specimen thickness are found in Figure 8.

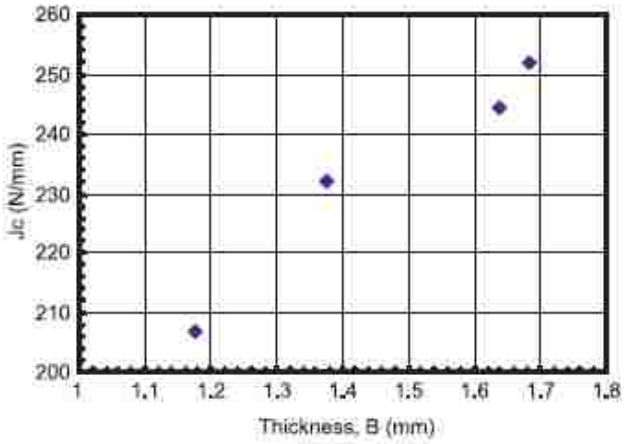

Figure 8: Variation of J fracture toughness with specimen thickness[14]

The change in J with respect to thickness shows that plane stress conditions prevail, and that the thickness influences the hydrostatic stress state and plastic zone within the material. Furthermore, in order for J_{IC} to be a single parameter for fracture toughness, plane strain conditions must be in use.

1.5.3 Crack Length Influences

Another influence on the fracture toughness of the sample is the crack length, or more specifically the ratio a/W, which is the ratio of the crack length (a) to the total height of the sample (W). Lereim and Embury[15] have shown that a/W causes fluctuations of J only up to a certain a/W ratio, after which, the J value remains constant.

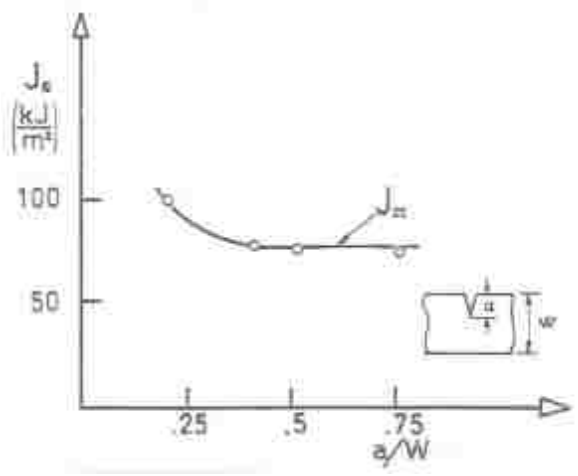

Figure 9: Influence of a/W ratio on J fracture toughness for HSLA steels[15]

The data in Figure 9 plateaus after a certain a/W value because as the crack length increases, the effective thickness of the sample increases as well, getting closer to plane strain conditions, and a single J_{IC} value independent of geometry.

Maiti and Keshbat[16] performed finite element calculations in order to show how the size and shape of the plastic zone changes during crack extension as well as during unloading. Figure 10 shows the progression of the three cycles of loading and unloading and the changes to the plastic zone.

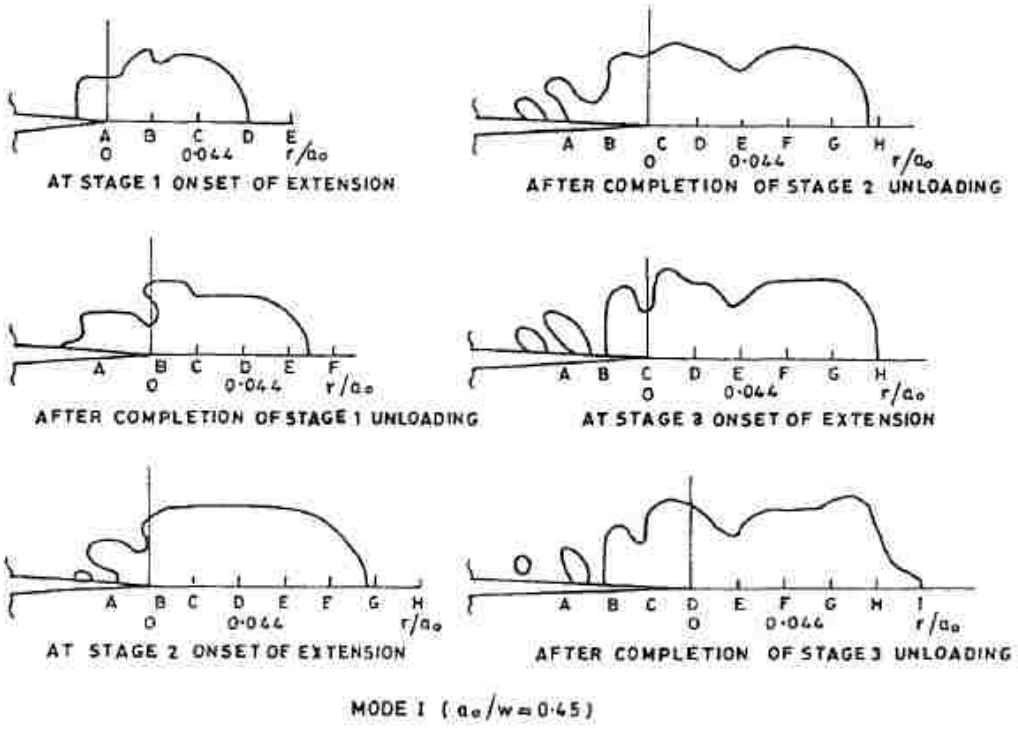

Figure 10: Plastic zones computed during three loading and unloading cycles undergoing fracture toughness finite element calculations[16]

As the crack propagates from point A at stage 1 to point D at stage 3, the spread of the plastic zone ahead of the crack tip is approximately $0.066a_o$ at initiation and $0.11a_o$ at unstable crack growth. The size of the plastic zone nearly doubles during the test simulation. The calculated J-integrals from the various FE tests of Maiti and Keshbat can be seen in Table 1.

Table 1: Calculated J-integrals at various cycles of crack extension[16]

a_0/w	Total extension $\Sigma\Delta a$ (mm) from initiation	Computed J (N.mm/mm^2) contours 1	2	3	4	J_{ave} (N.mm/mm^2)
0.45	0.0	8.757	8.739	8.800	8.803	8.775
	0.4	13.236	13.191	13.205	13.237	13.216
	0.8	15.012	15.024	15.166	15.199	15.100
	1.2			16.863	16.791	16.823
0.50	0.0	8.905	8.960	9.016	9.019	8.995
	0.4	13.061	13.064	13.036	13.075	13.060
0.55	0.0	8.938	8.914	8.970	8.972	8.948
	0.4	12.969	12.969	12.982	12.982	12.975

The data in the table shows four separate J-integral contours calculated for different initial a/W values and at different crack extensions. It is important to note that the J-integrals calculated are more or less the same along all contours, which should be the case because, as mentioned earlier, path independence is one of the requirements of the J-integral.

Although it has been shown that sample configuration and geometry, thickness, and crack length all affect the J integral, it can still be used as a single parameter criterion for fracture toughness when the sample is tested under plane strain conditions. Landes and Begley[9] have stated that the size of the remaining ligament must be sufficiently large in comparison to the plastic zone that resulted during the test, and as was shown in Figure 1 and Equation 2, the size of the plastic zone under plane stress conditions is three times larger than plane strain. They have also concluded that the local crack tip singularity due to plasticity and blunting of the crack tip overrides the effect of slip line fields in determining J_{IC}.

1.6 Fracture Toughness of Copper Precipitation Strengthened Steels

The history behind the development of copper precipitation strengthened steels and their use in naval ship hulls has been covered extensively by Czyryca.[17] According to Czyryca,

welding is the greatest cost driver and the largest single contributor to shipyard labor. Fabrication of the hull, which includes materials, welding, and nondestructive evaluation, can be as high as 20% of the total cost of the entire ship. With this is mind, it is crucial to understand the behavior of the various regions of the HAZ in the weld in order to prevent failures from occurring.

1.6.1 Dislocation Motion Effects on Fracture Toughness

Much of the J fracture toughness work occurs on the 'upper shelf' of impact energy versus temperature curves. This is the region in which the material exhibits fully ductile behavior and where plastic deformation ahead of a crack tip will be the highest. Ericksonkirk et al.[18] have said that there are two major contributions to deformation due to dislocation motion. The dislocation motion due to temperature change constitutes the thermal effects, and the influence of second-phase particles on the ability of the matrix to allow dislocation motion constitutes the non-thermal effects. These two effects alter the fracture toughness of a material. The thermal effects control the dislocation motion through the crystal lattice by altering the vibration of the atoms and as the temperature increases, the vibration increases, thus providing greater space for the dislocations to move. As these dislocations move through the lattice they will inevitably interact with microstructural inhomogeneities, namely second-phase particles and the nature of this interaction will also contribute to the fracture toughness of the material. Cleavage fracture occurs when ductile behavior is no longer exhibited by the material, and the fracture toughness is a measure of the energy absorbed by the motion of dislocations before they pile up at a second phase particle leading to unstable cleavage fracture. The opposite mode of failure occurs when there is sufficient pile up of dislocations at a second

phase particle such that voids are able to nucleate and link up leading to ductile failure of the material. This ductile fracture is the mode typically seen in the 'upper shelf' region of impact toughness curves.

1.6.2 Effect of Copper Additions

The effect on fracture toughness of copper additions to HSLA steels has been shown to have a positive correlation in most cases. Lis et al.[19] took HSLA-100 and altered the composition such that the copper composition was raised from 1.6wt% to 2.0wt% at the expense of iron. As seen in Figure 11 the HSLA-100 with 2wt% copper exhibited higher fracture toughness at all yield strength levels, up to approximately 1000MPa.

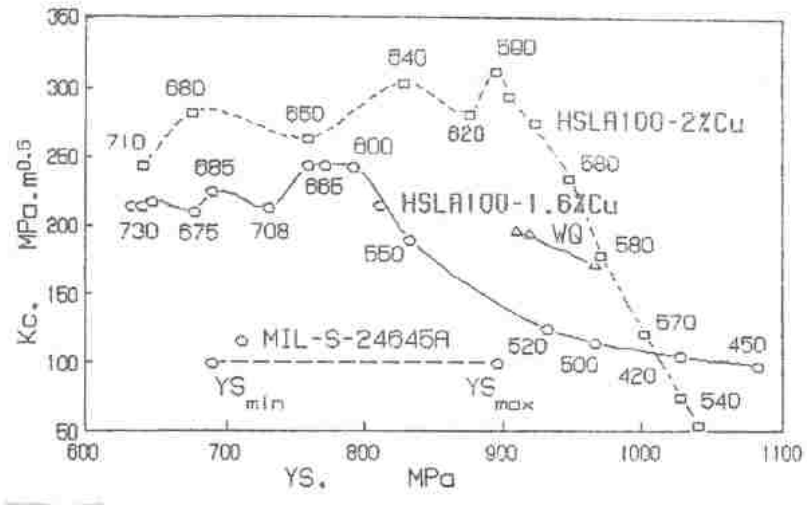

Figure 11: Fracture toughness as a function of strength level for HSLA-100 steels with varying copper content. The numbers on the plot indicate the ageing temperatures in °C following water quenching.[19]

Lis attributes this increase to the nature of the copper precipitates and their influence on formation of austenite. HSLA-100 in the overaged condition results in incoherent ε-Cu precipitates, and these precipitates allow for easier formation of new stable austenite, which

can provide a strong barrier to growth of cleavage cracks in the ferrite matrix. The influence of carbon equivalent within these stable austenite structures was also observed and is shown in Figure 12.

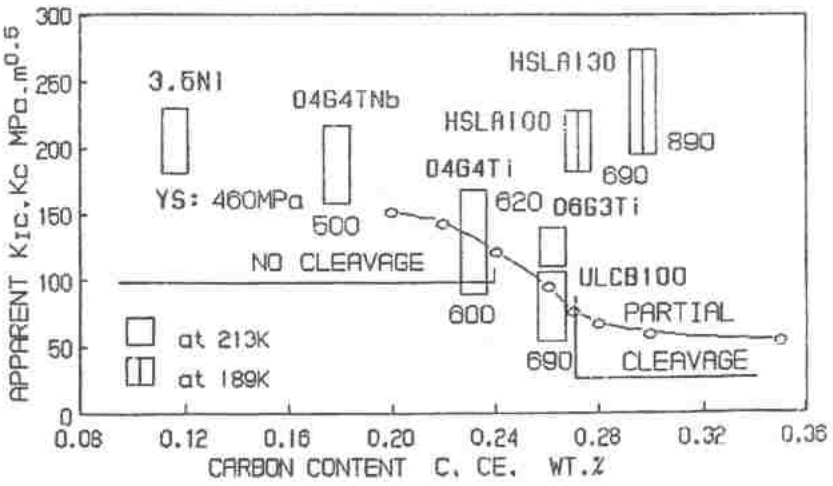

Figure 12: Fracture toughness as a function of carbon equivalent within stable austenite phases compared to data seen for a variety of steels.[19]

The increase in fracture toughness at lower carbon equivalents is hypothesized to come from enhanced ductility caused by a strain induced phase transformation from γ – α' and the energy dissipated by the austenite at the crack tip.

For copper precipitation steels, the morphology of the copper precipitates plays a strong role in how the steel is strengthened, and its importance within the HAZ cannot be overlooked. Reports have shown that copper acts as a solid solution strengthener when its content is lower than 0.5wt% and as a precipitation strengthener at levels above this value. The results of Tomita et al.[20] show that, for an alloy with 0.9wt% Cu, 5°C/min is the critical cooling rate for the precipitation of copper to occur. Figure 13 shows the hardness change as a function of cooling time from 800°C to 500°C. The hardness change remains constant for cooling times up to

$3.6x10^3$ sec, which is a cooling rate of approximately 5°C/min. At longer cooling times, the hardness change is less. This suggests that precipitation of copper does not occur at cooling rates above 5°C/min in this particular alloy system.

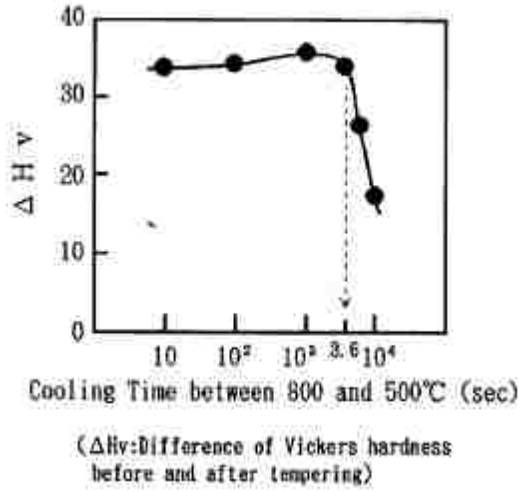

Figure 13: Relationship between hardness change (before and after tempering) to the cooling time (T8-5)[20]

Das et al.[21] performed J fracture toughness tests on HSLA-100, which has low amounts of carbon (0.04wt%) and higher amounts of copper (1.6wt%). The carbon content is intentionally kept low in order to improve weldability, and due to this reduction the copper content is increased in order to regain some of the strength by increasing the amount of precipitation strengthening. The copper precipitates initially form as coherent nanoscale particles at approximately 500°C, then coarsen and become incoherent at higher and higher temperatures. Figure 14 shows the influence of different processing conditions on the microstructure of the HSLA-100 steel.

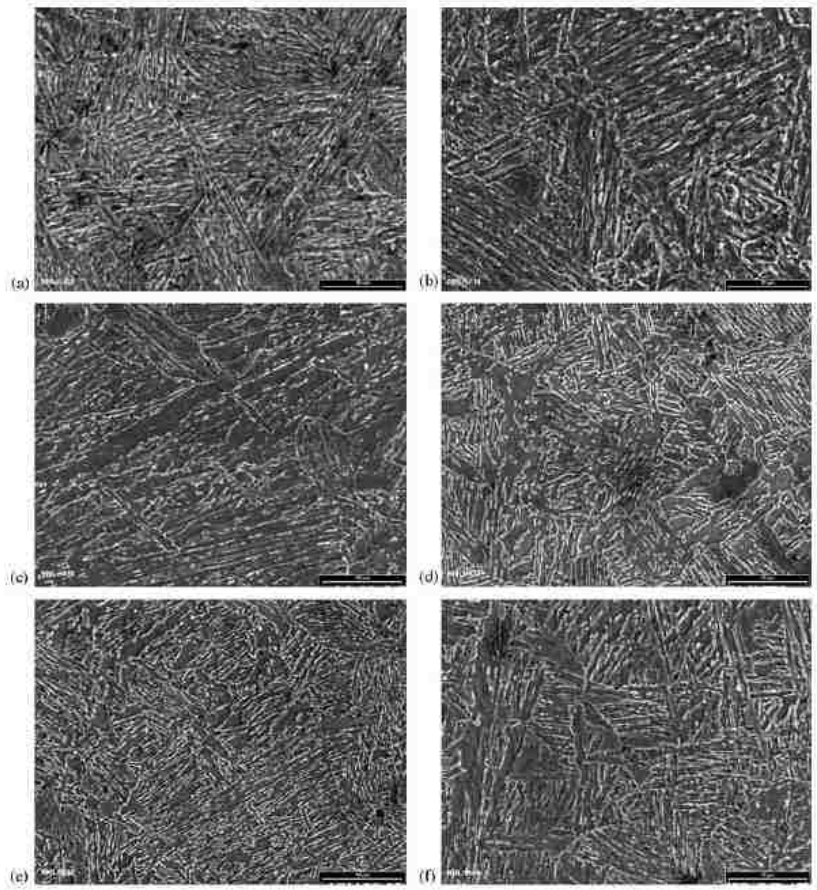

Figure 14: SEM micrographs showing the influence of processing conditions on the microstructure of HSLA-100 (a) water quenched (WQ), (b) WQ and aged at 400°C, (c) WQ and aged at 500°C, (d) WQ and aged at 600°C, (e) WQ and aged at 650°C, (f) WQ and aged at 700°C[21]

The structure is acicular in all cases with some gradual coarsening as the ageing temperature increases. The changes in microstructure do not give the full picture of what is happening in the material as the nanoscale precipitates are also a factor in the fracture toughness. The J fracture toughness for a variety of ageing temperatures can be seen in Figure 15.

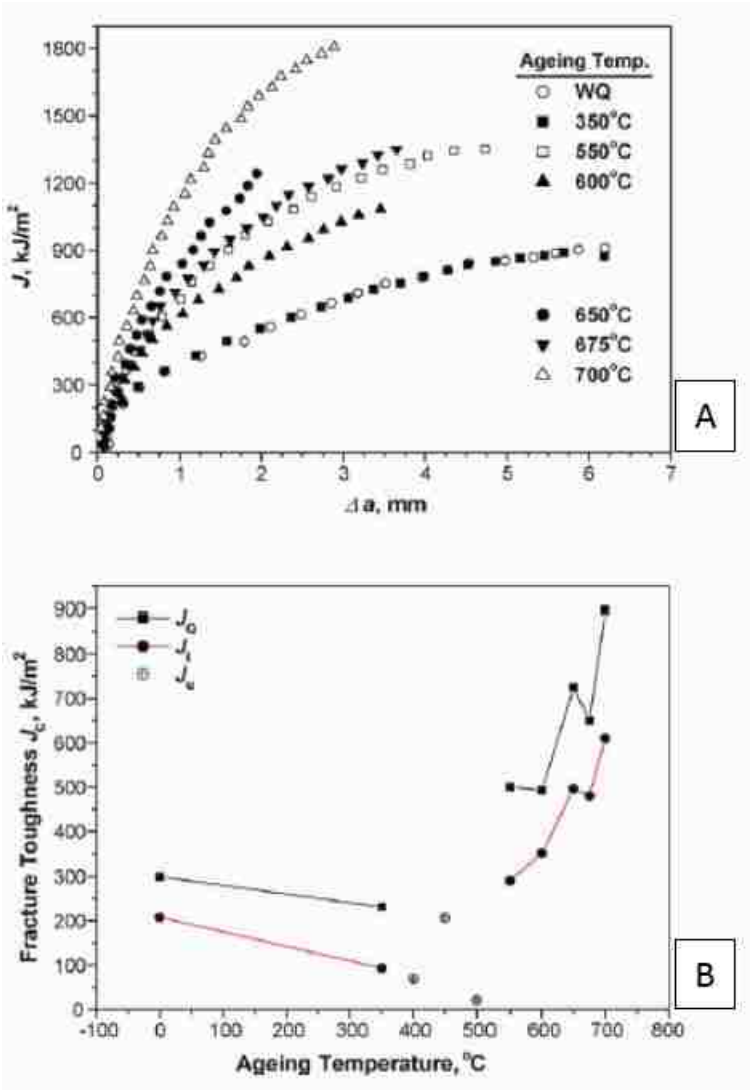

Figure 15: (a) JR Curves for differing ageing temperatures in HSLA-100 steel, (b) Fracture toughness as a function of ageing temperature in HSLA-100 steel[21]

The fracture toughness is a minimum in the WQ condition and also at the 550°C ageing temperature. The minimum in the WQ condition is due to the presence of untempered martensite, whereas the minimum at the 550°C peak temperature is due to the fact that the copper precipitates are coherent with the matrix. The increase in fracture toughness at higher ageing temperatures is partly due to tempering of the martensite, but mostly due to the copper precipitates losing coherency with the matrix. Copper precipitate coherency, as implied by

mechanical property variations seen by Das[21], restricts plastic deformation which, in turn, limits the formation and growth of microvoids leading to a decrease in ductile fracture.

1.6.3 Fracture Toughness of Thermally Simulated Heat Affected Zones

Shi and Han[22] have performed work similar to the scope of this study, but on a different type of HSLA steel. They used a Gleeble to simulate various regions within the HAZ of a weld, and then performed J fracture toughness tests in order to correlate the HAZ microstructure to the toughness properties. Their results (Figure 16) showed that a cooling time (T8-5) of approximately 18s yielded the highest fracture toughness, and times of over 45s significantly reduced the fracture toughness of the material.

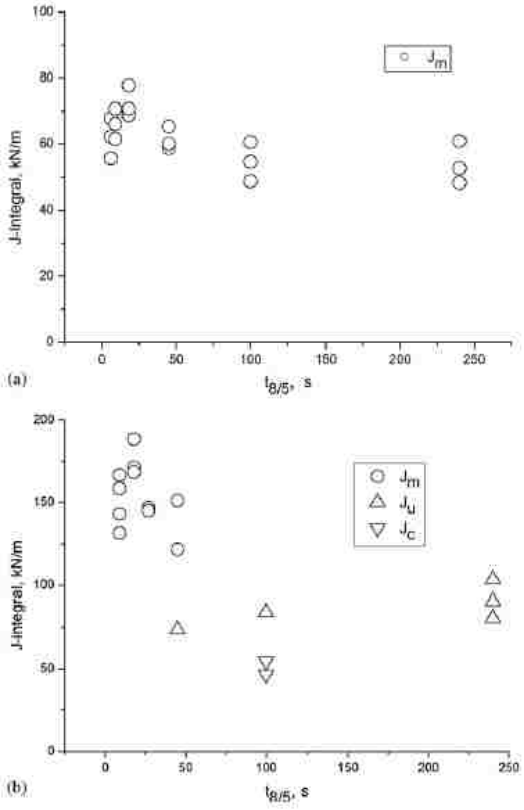

Figure 16: Effect of cooling time on the fracture toughness in the (a) T-L orientation and (b) L-T orientation[22]

Their work also showed the influence of different peak temperatures which correspond to different areas within the HAZ. The results are shown in Figure 17.

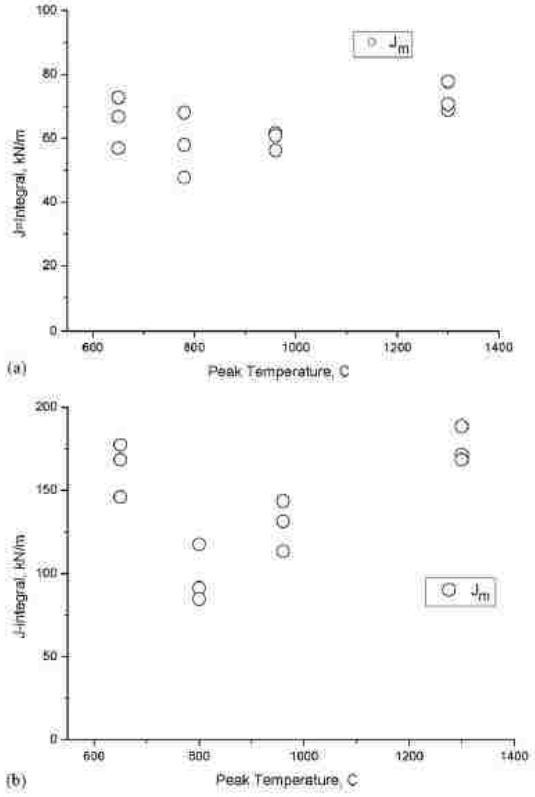

Figure 17: Effect of peak temperature on the fracture toughness in the (a) T-L orientation and (b) L-T orientation[22]

The mixed microstructure of martensite and austenite (MA constituent) formed at the 800°C peak temperature showed the lowest fracture toughness of all the peak temperatures. Shi and Han proposed that this was due to the dissolution of carbides at the grain boundary and partial transformation to austenite. The austenite formed in this region of the HAZ is only partly transformed due to the 800°C peak temperature. The low temperature makes diffusion of

carbon very difficult, thus, the grain boundaries are rich in carbon and the MA constituent creating an easy path for fracture.

1.7 Role of Second Phase Particles on Fracture Toughness

The initiation of ductile fracture is caused by the nucleation and growth of voids at second phase particles. In steels, the second phase particles are either carbides or sulfide or silicate inclusions. In the case of nonmetallic inclusions, there are two possible influences: they can provide an inert surface, which can aid in the nucleation of acicular ferrite, increasing the strength and toughness of the material or can they can be initiation sites for ductile and cleavage fracture. The mode in which these nonmetallic inclusions act is dependent on their chemistry and their size.[23]

Once a void is nucleated at a second phase particle the void will pass through the boundary between the particle and the surrounding matrix, and then propagate through the grain and to the next grain boundary where it could link up with other such cracks.[24] These cracks will elongate in the direction of an applied tensile stress, but will need a shear component if they are to move laterally within the material and link up with other cracks to form a microneck. The micronecks will eventually grow apart from each other leading to ductile fracture with highly dimpled fracture surfaces. This link up of voids can be seen in Figure 18.[3]

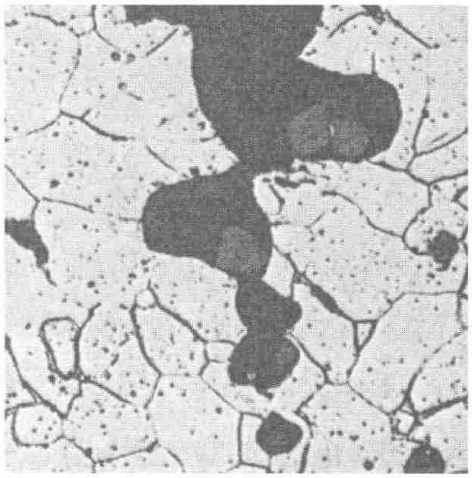

Figure 18: Growth and link up of microvoids to form a ductile crack in a free-cutting mild steel.[3]

1.7.1 Influence of Stress Triaxiality

Chae et al.[25] performed studies on the failure behavior of HAZ in HSLA-100 and HY-100 steels, and found that the failure mode was influenced by the triaxial stress state in the material. For low stress triaxialities the failure was dominated by microvoid coalescence (equiaxed voids grow to impingement) seen in Figure 19a, whereas for high stress triaxialities the void sheet mode (links elongated inclusion initiated voids by a shear instability) seen in Figure 19b and a small amount of cleavage fracture seen in Figure 19c were the dominant modes of failure.

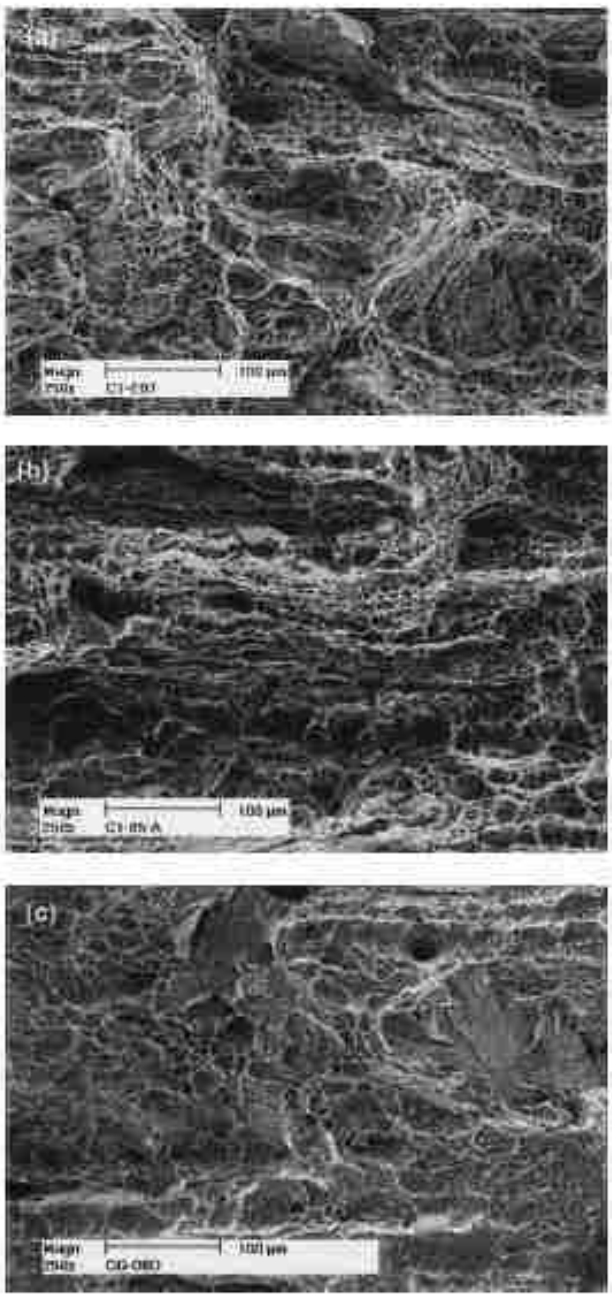

Figure 19: SEM micrographs of the fracture surfaces the coarse grained HAZ of HY-100 with stress triaxiality increasing from A to C.[25]

1.7.2 Influence of Manganese Sulfide (MnS) Inclusions

Kiessling[3] has divided steel inclusions into five separate categories based upon the deformation behavior of the inclusions, but only manganese sulfide (MnS) inclusions will be discussed here. These inclusions are separated into three types based upon differences in their morphology as seen in Figure 20. A type I MnS inclusion is globular and is only formed when oxygen is present in the melt of the material. Type II inclusions are of the interdendritic eutectic form, and Type III are random angular particles.[3]

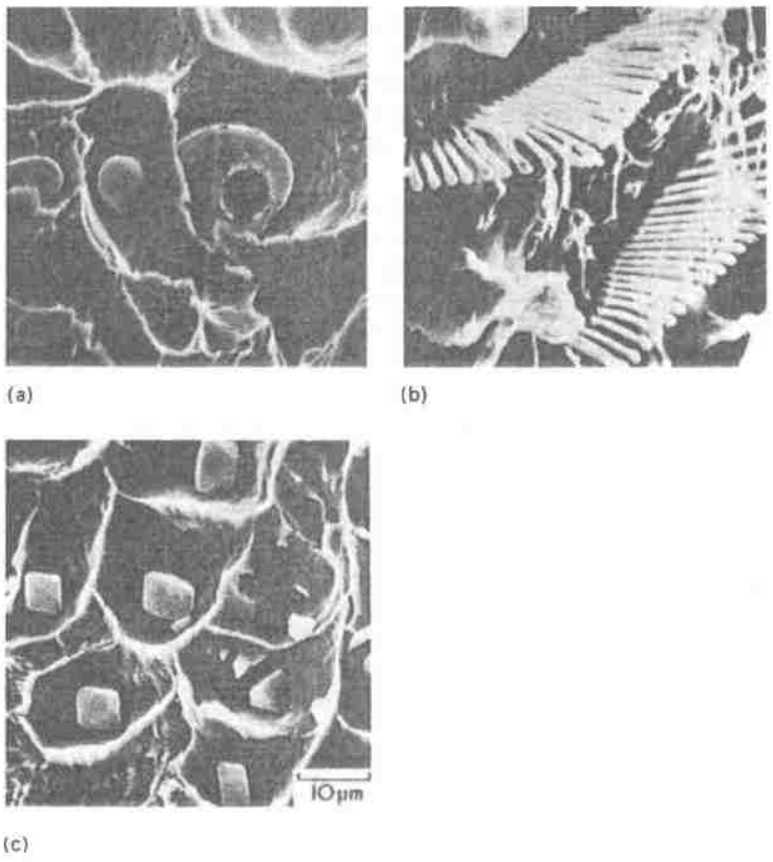

Figure 20: SEM micrographs showing the various morphologies of MnS inclusions (a) Type I (b) Type II (c) Type III[3]

MnS inclusions can play a critical role in the failure of some steels. Chae et al.[26] have linked the void sheet mode of failure to the presence of MnS inclusions, which are preferentially located in granular ferrite layers of a banded HY-100 steel. The inclusions provide easy initiation sites for large elongated voids that trigger localized deformation between the banded layers of granular ferrite. The inclusions also influence cleavage fracture as well because they contract more than the surrounding matrix during cooling from hot working temperatures. This over contraction creates a stress concentration at the particle matrix interface making it a prime site for debonding and void nucleation.[27]

1.7.3. Particle Size Effects on Fracture Toughness

Bhadeshia states that an inclusion's effectiveness at initiating ductile cracks increases above a critical size range. A larger (coarser) particle will create a higher stress concentration at its boundary, which will lead to localized rupture and microcracking. This is supported by the work of Chae[25] and also Ishikawa[28]. The results of Chae showed that the inclusion content of the HY-100 steel and its 100S weld metal control the ductile fracture behavior, and Ishikawa demonstrated that the fracture toughness of a specific type of steel was lowered by increasing initiation site size (Figure 21).

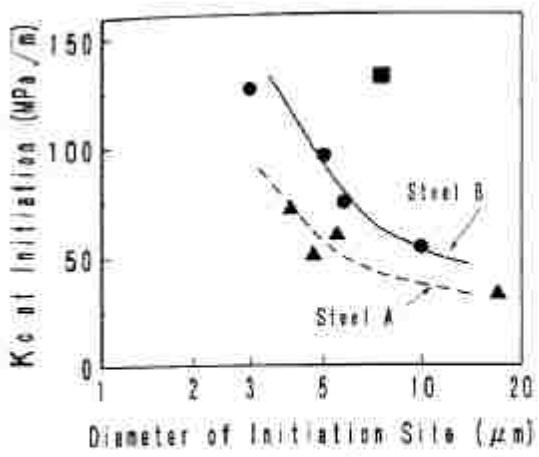

Figure 21: Relationship between initiation fracture toughness and the size of the initiation site.[28]

1.7.4 Influence of Carbides

MnS inclusions are not the only second phase particles present in steels and various morphologies of carbides are also of importance. A cementite sphere of similar size to a MnS particle was shown to be stronger, and does not crack or debond at small strains.[3] This result lends itself to the understanding that these carbides can appreciably deform without nucleating any voids which leads to good ductility and toughness. In comparison, lamellar cementite also does not crack at small strains, but exhibits lower ductility than spheroidal cementite, as seen in Figure 22. This is because when the lamellar cementite cracks, the crack is able to quickly run the length of the lamella leading to well defined cracks in the pearlite colony.[3]

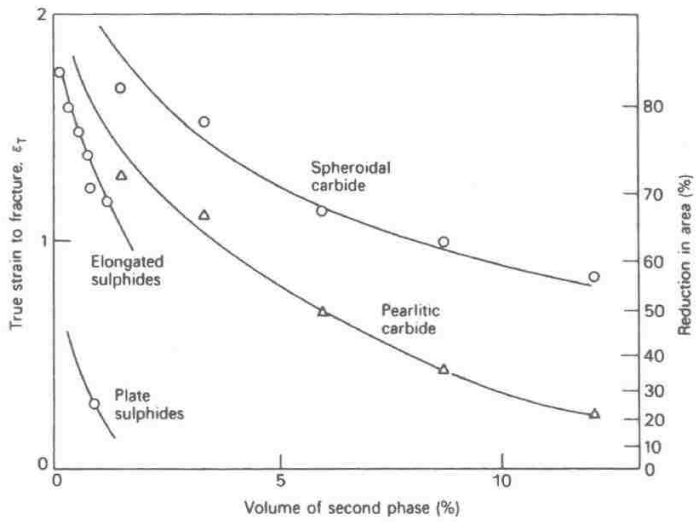

Figure 22: Effect of second phase particles on the ductility of steel[3]

1.7.5 Influence of Second-Phase Microstructure

Second-phase within the microstructure also plays an important role in the ductility and toughness of a material, being influenced by hard constituents along grain boundaries, harder phases next to softer ones, etc. The work of Chae et. al.[26] looked at the banded microstructure within HY-100 steel, which had bands of granular ferrite and bands of equiaxed ferrite. The failure mode of the material shows that slip accommodation occurs within the equiaxed ferrite layer in order to accommodate the deformation characteristics of the harder neighboring granular ferrite layer (Figure 23). These results show that plasticity is constrained by the granular ferrite along the long dimension of the band.

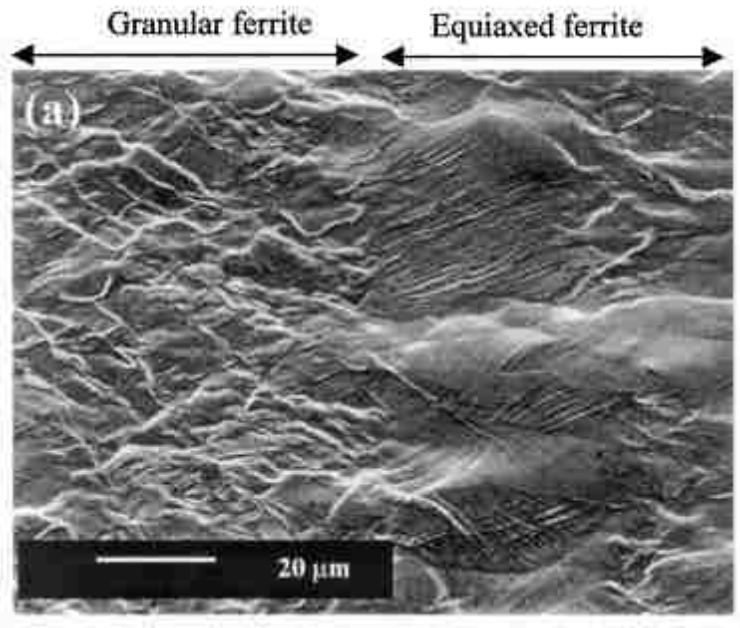

Figure 23: Plastic deformation within neighboring bands of granular ferrite and equiaxed ferrite in HY-100 steel[26]

Many HSLA steels have compositions and microstructures that are susceptible to forming hard brittle constituents at the grain boundaries in the CGHAZ. Depending on alloy composition and weld thermal cycle, the first pass of a welding operation may yield upper bainite with a large prior austenite grain size. A second pass will further heat this area to the intercritical region, where the austenite will nucleate and grow along the bainite lath boundaries and the prior austenite grain boundaries. After nucleation it will become enriched with carbon, which when cooled will transform into a hard and brittle constituent. This can be seen in Figure 24 for an HSLA type steel containing 0.083wt% C after a multipass thermal cycle. The material was heated to 1350°C at a rate of 200°C/s, with a t8-5 of 30s, and an interpass temperature of 200°C. The peak temperature of the second pass varied, leading to the different microstructures seen in Figure 24.

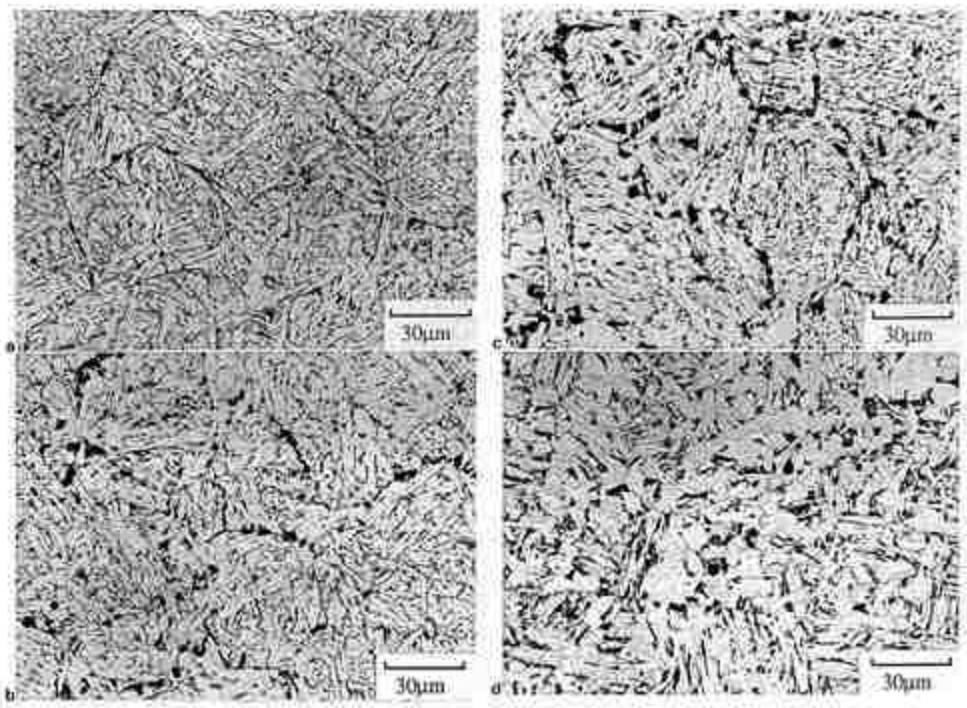

Figure 24: Microstructure of HSLA steel showing increasing amounts of blocky MA constituent at the grain boundaries after intercritical heating on the second pass to (a) 764°C (b) 778°C (c) 785°C and (d) 804°C[27]

The formation of this hard MA constituent caused a drop in the toughness of the material because of the lack of ductility at the grain boundary (Figure 25).

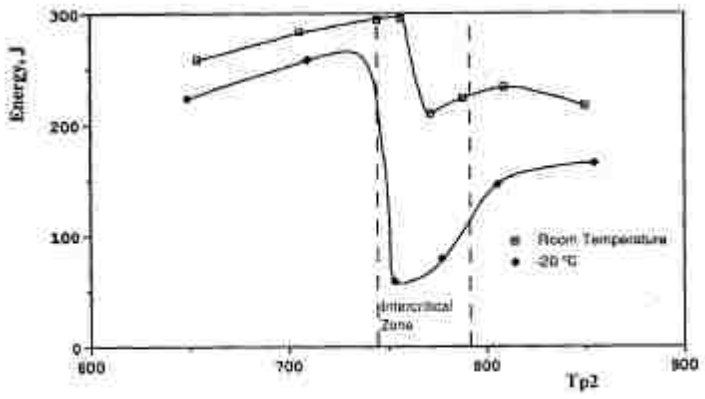

Figure 25: Impact energy as a function of temperature showing low toughness in the intercritically heated region[27]

The fracture surface of this material (Figure 26) shows that the cracks run along the prior austenite grain boundaries and can originate at a region where a blocky MA particle has become debonded from the surrounding matrix.

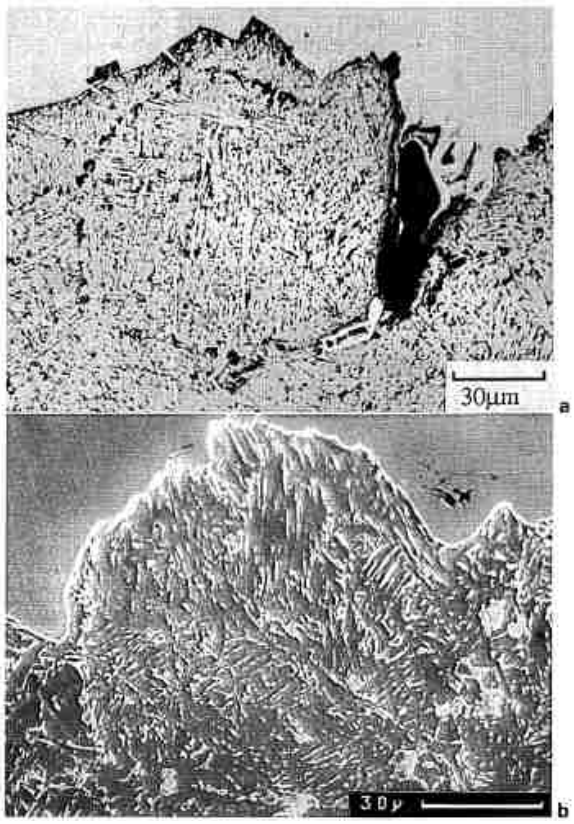

Figure 26: Cross section of charpy fracture surface in which the failure runs along the prior austenite grain boundaries after originating at debonded MA constituent (dark spot in A).[27]

To further illustrate the conclusion that the MA constituent is the cause of failure, Davis and King[27] also slowed the cooling rate after the second weld pass in order to suppress its formation, instead forming upper bainite and pearlite regions. The results (Figure 27) show that no reduction in toughness is observed, whereas for higher cooling rates (formation of the MA constituent) a drop in toughness is seen at the intercritically heated region.

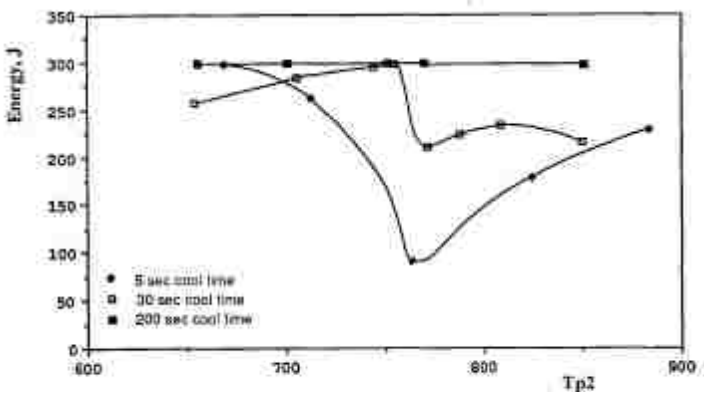

Figure 27: Impact energy as a function of temperature for various cooling times after the second weld pass[27]

A proposed mechanism for the toughening of a high-strength low alloy steel via bainite formation was given by Tomita.[29] When a ductile second phase appears in acicular form, such as lower bainite, it can partition the prior austenite grains of the matrix martensite, and if this partition occurs the strength can be improved due to the refinement of the martensitic substructure as well as plastic restraining of the bainite by the martensite. In contrast, however, when the second phase appears as a mass and fills the prior austenite grain boundaries of the matrix, such as upper bainite, strength is decreased. This is caused by a non-uniform strain between the bainite and the martensite during earlier deformation.

1.8 Experimental Objective

It is unknown how the fracture toughness of NUCu-140 is altered in the HAZ following an arc welding process. It is the goal of this research to simulate four different regions in the HAZ, each corresponding to a different peak temperature, and perform J fracture toughness tests. The trend in fracture toughness needs to be correlated to the microstructural changes as well as the changes in copper precipitate morphology.

2. Experimental Procedure

The chemical composition of NUCu-140 can be seen in Table 2. The alloy was given an initial homogenization heat treatment at 1150°C for 3 hours. The alloy was then hot cross-rolled at 950°C and air cooled. Next, the plates were solutionized at 900°C for 1 hour, water quenched, and then aged at 550°C for 2 hours and air cooled. The chemical composition of NUCu-140 can be seen in.

Table 2: Chemical composition of NUCu-140 (all values in wt%).

Element	NUCu-140
Al	0.65
C	0.04
Cu	1.35
Fe	Bal.
Mn	0.47
Nb	0.07
Ni	2.75
P	0.009
S	0.002
Si	0.47

Thermal simulations were conducted on a Gleeble 3500 series thermo-mechanical simulator. The thermal cycles were derived from calculations done using Sandia Optimization and Analysis and Routine (SOAR)[30] representative of a 750J/mm heat input, and were controlled using the

Gleeble QuikSim software package. The specific peak temperatures were chosen in order to obtain samples heated to the subcritical (675°C), intercritical (800°C), fully recrystallized (900°C), and coarse-grained (1350°C) heat affected zone regions. These peak temperatures were determined by dilatometry experiments by Farren et al.[1] in order to establish the Ac1 and Ac3 temperatures. Samples examined under a light optical microscope were prepared using standard metallographic techniques and etched using 3% nital. Microhardness was performed on a LECO M400-FT tester using a Vickers indenter, 300g load, 15s dwell time, and measurements were done using NewAge CAMSWin program. Grain size was conducted according to ASTM E-112[31] standards using the three circle method, and 5 fields were measured for each sample. Fracture toughness testing using the J-integral was performed according to ASTME-1820[32], with a single edge notched bend (SENB) sample of size 8x16x80mm (Figure 28), with a machined notch of 4mm. An average and standard deviation were calculated from five tests for each material condition.

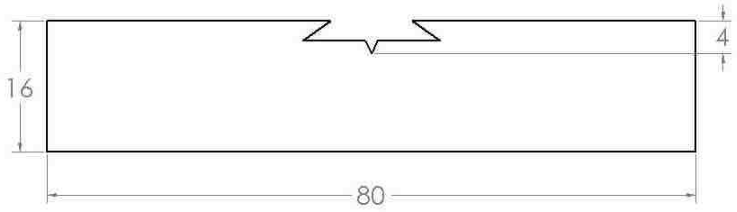

Figure 28: Dimension of fracture toughness bar used for testing. All dimensions are in mm, and the sample is 8mm thick.

Pre-cracking was conducted on a servo-hydraulic Instron frame, with a clip gage attached to the sample and interfaced with the machine. The pre-crack was induced at a frequency of 10Hz until the a/W ratio was 0.5. Fracture toughness testing was performed in displacement control on an Instron 5567 load frame using a resistance curve test method with a span of 65mm. Each

cycle was as follows: load 0.075mm then unload 0.025mm at a rate of 0.25mm/min. Fracture surfaces were observed on an FEI XL-30 SEM using an accelerating voltage of 15kV, and energy dispersive spectroscopy (EDS) analysis and imaging of particles was performed on a Hitachi 4300SE/N SEM using an accelerating voltage of 15kV.

3. Results and Discussion

3.1 Microstructure of Gleeble Thermal Simulations

The microstructures associated with each thermal cycle can be seen in Figure 29. Figure 29(a)-(d) shows a microstructure consisting of equiaxed ferrite, while the microstructure produced from the 1350°C peak temperature (Figure 29(e)), exhibits a more complex microstructure with regions of acicular ferrite, bainite, and possibly martensite.

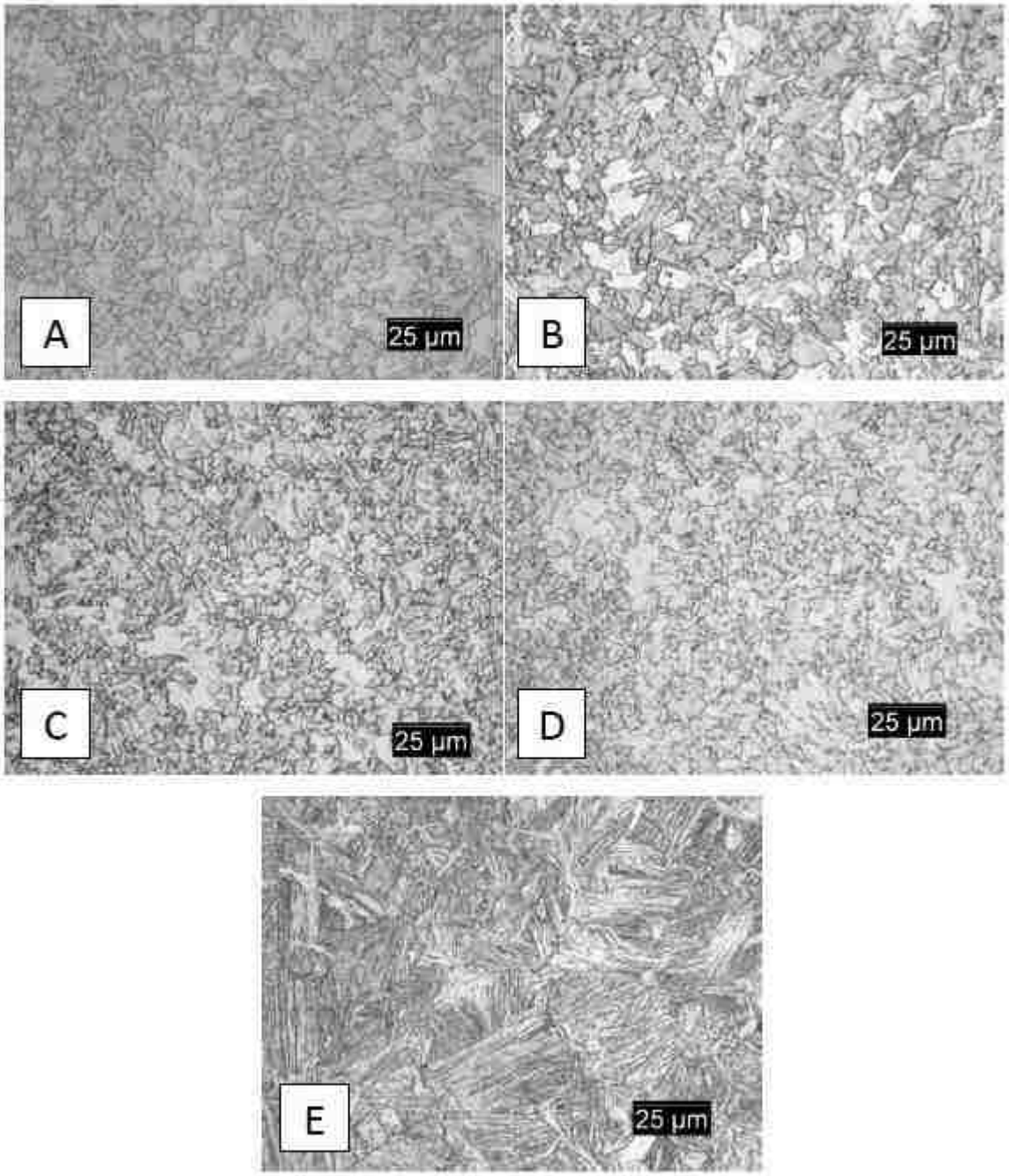

Figure 29: Light optical micrographs of NUCu-140 showing an equiaxed ferrite microstructure for peak temperatures of (a) base metal, (b) 675°C, (c) 800°C, and (d) 900°C. (e) The 1350°C peak temperature microstructure consists of acicular ferrite, bainite, and martensite. Etched with 3% nital.

3.2 Grain Size of Simulated HAZ Samples

Figure 30 shows the results of the grain size measurements for the base metal and the four thermally simulated regions. There is very little difference between the base metal and the peak temperatures of 675, 800, and 900°C, but there is a large increase in grain size for the 1350°C sample. The grain size of the 1350°C samples are a prior austenite grain size, whereas the other samples were equiaxed ferrite.

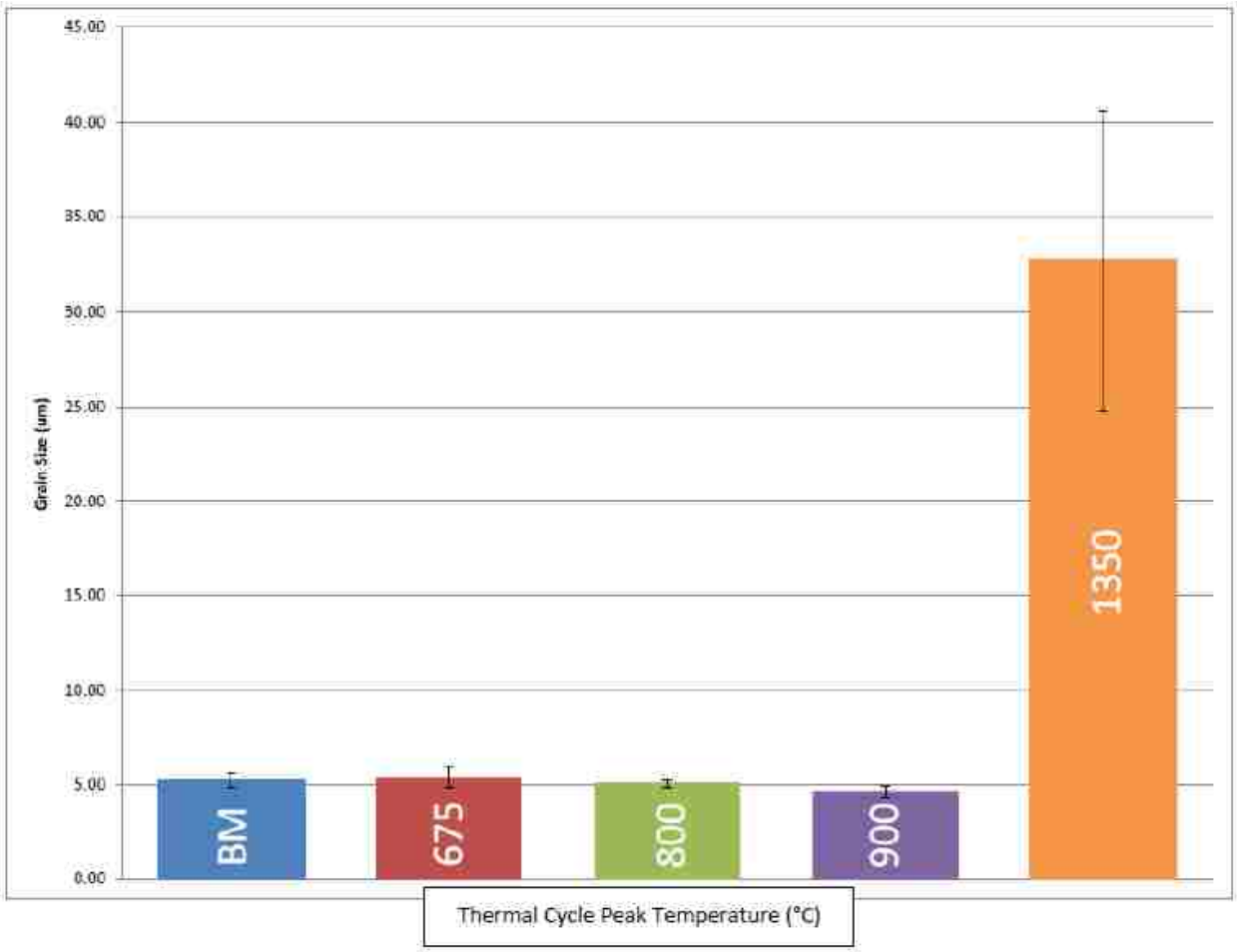

Figure 30: Grain size measurements for NUCu-140 HAZ thermal simulations.

3.3 Microhardness of Simulated HAZ Samples

The Vickers microhardness, seen in Figure 31, shows a decrease from the base metal (295HV) to the minimum hardness of 228HV seen in the 900°C peak temperature, followed by an increase to the peak hardness of 305HV seen in the 1350°C peak temperature sample.

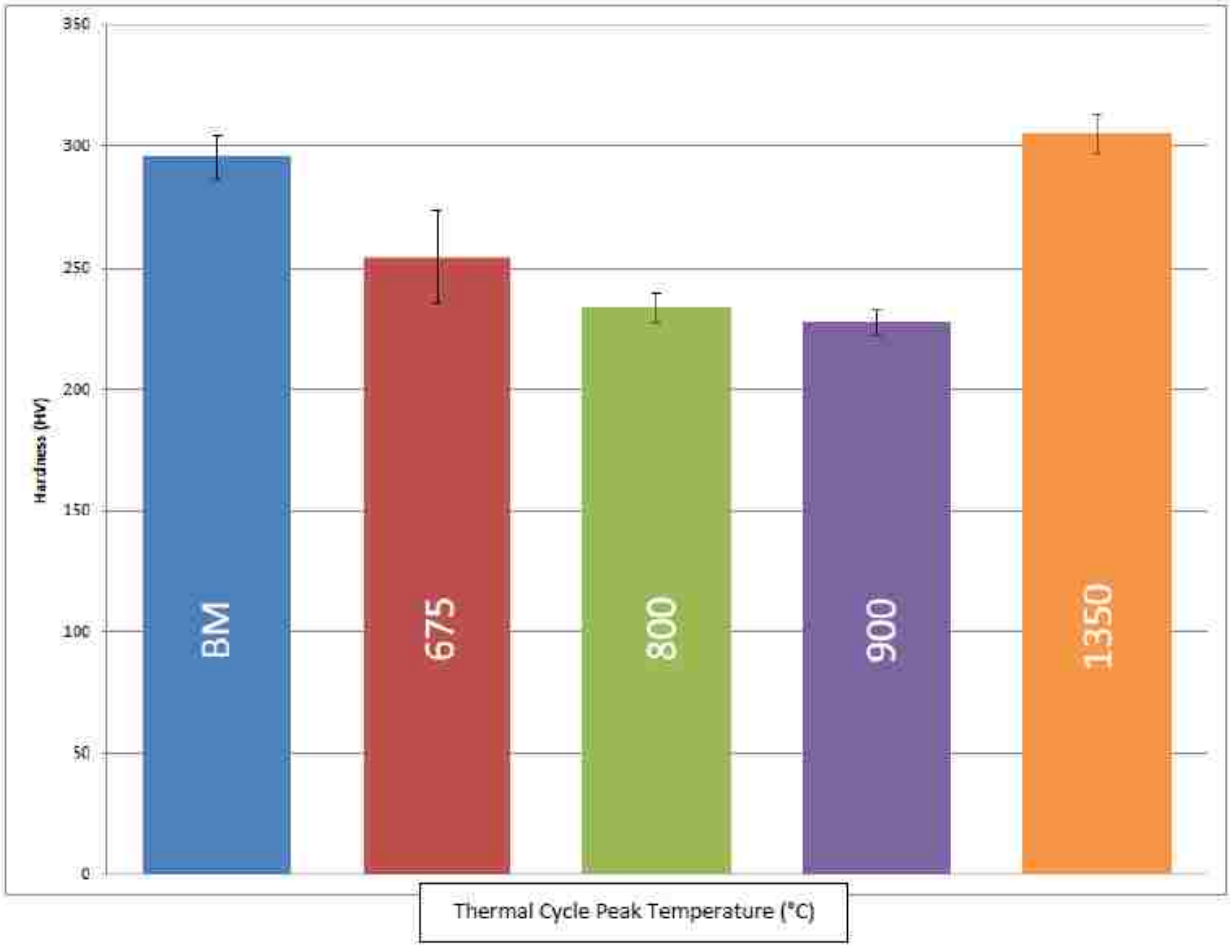

Figure 31: Vickers microhardness of NUCu-140 HAZ thermal simulations.

3.4 Fracture Toughness of Simulated HAZ Samples

The results of the fracture toughness tests are shown in Figure 32 and Figure 33. Figure 32 shows representative J-R curves for each of the thermal cycles and the base metal plotted as

data points along with the ASTM required exclusion lines. The results of all of the fracture toughness tests are plotted in Figure 33 as averages with error bars. These results show that the base metal has the lowest fracture toughness (J_Q) of 224kJ/m^2 increasing up to the maximum of 425kJ/m^2 at the 900°C peak temperature, followed by a decrease to 255kJ/m^2 at the 1350°C peak temperature. According to ASTM standard E1820, these J_Q values meet the criteria to be classified as J_{IC}.

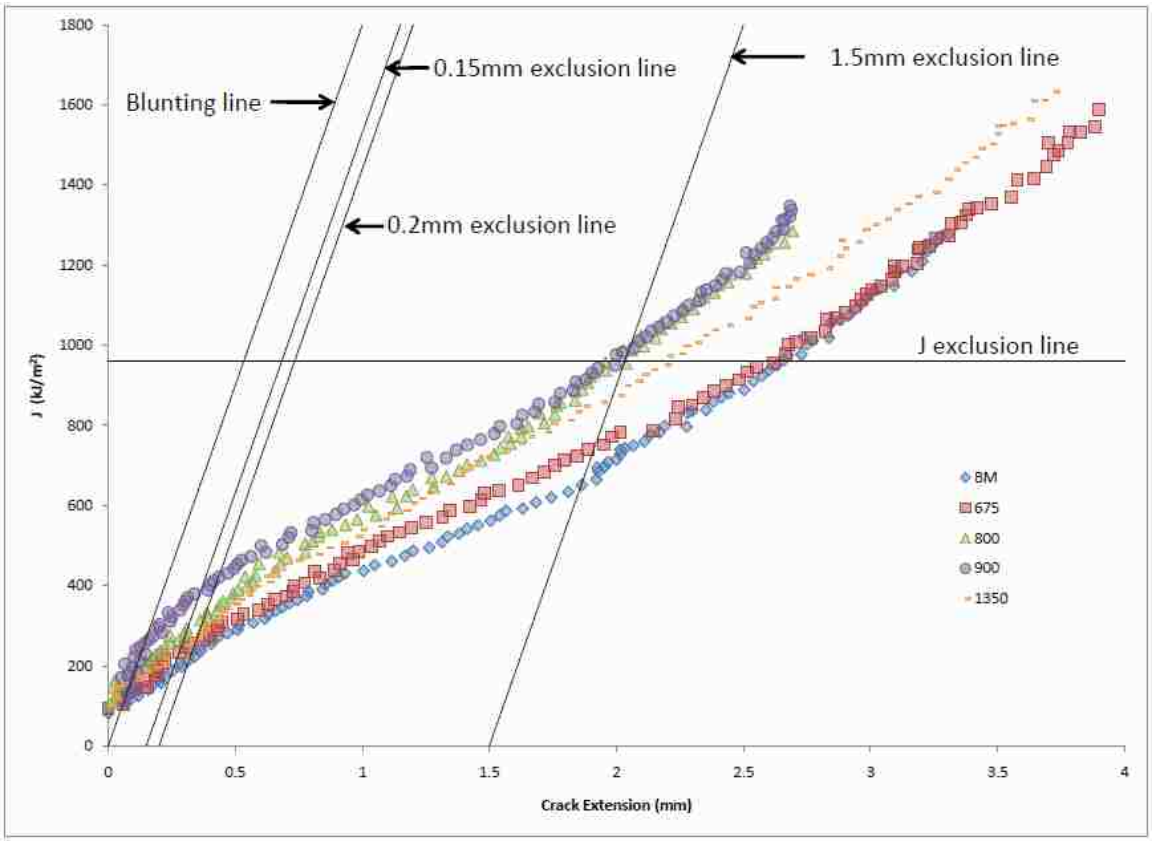

Figure 32: Crack growth resistance curves (J-R curves) for NUCu-140 thermal simulations.

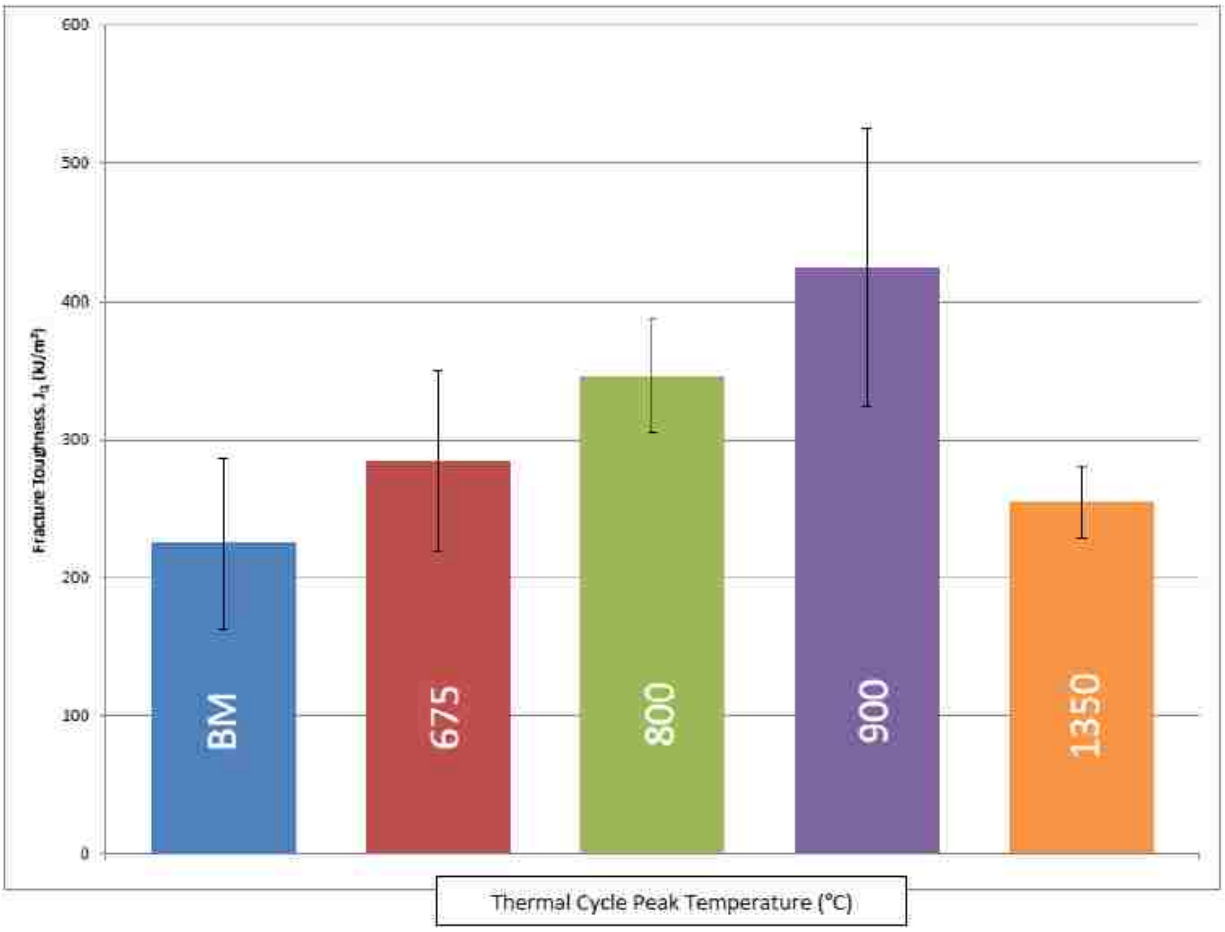

Figure 33: Average fracture toughness values (J_Q) of NUCu-140 thermal simulations showing a maximum at the 900°C peak temperature.

3.5 Fractography of Simulated HAZ Samples

The fracture surfaces of each of the samples are presented in Figure 34 and Figure 35. Figure 34 shows low magnification SEM images of the entire fracture surface of each sample displaying microcracks oriented in the direction of primary crack growth. The higher magnification images seen in Figure 35 show a failure mode of microvoid coalescence for the base metal, 675°C, 800°C, and 900°C peak temperatures (Figure 35(a)-(d), respectively). The

1350°C peak temperature samples (Figure 35(e)) displayed a mixed more of microvoid coalescence and cleavage fracture.

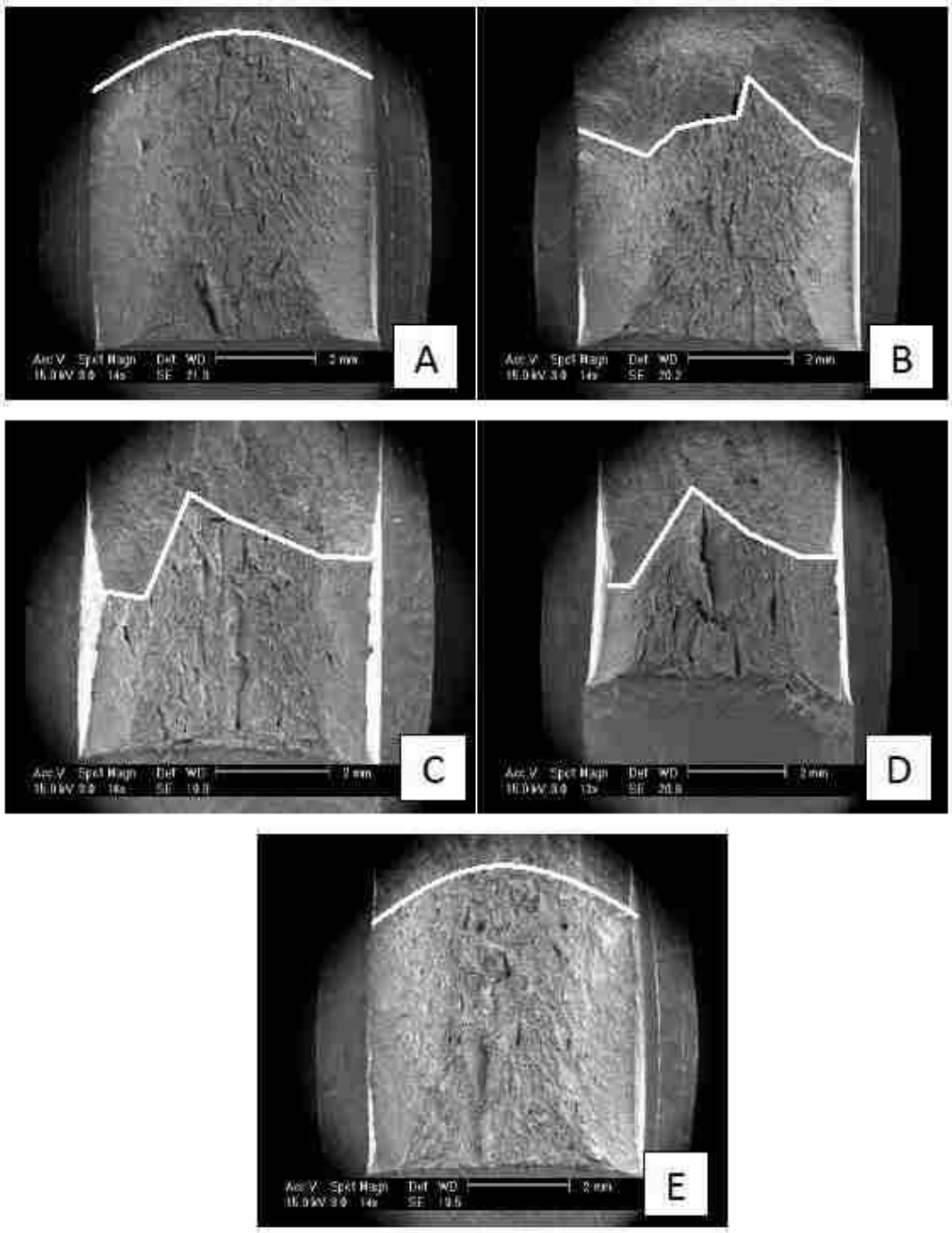

Figure 34: Low magnification SEM images of fracture surfaces for (a) NUCu-140 base metal, and thermal simulations with peak temperatures of (b) 675°C, (c) 800°C, (d) 900°C, and (e) 1350°C. Note that the fracture surface above the white line was induced following testing.

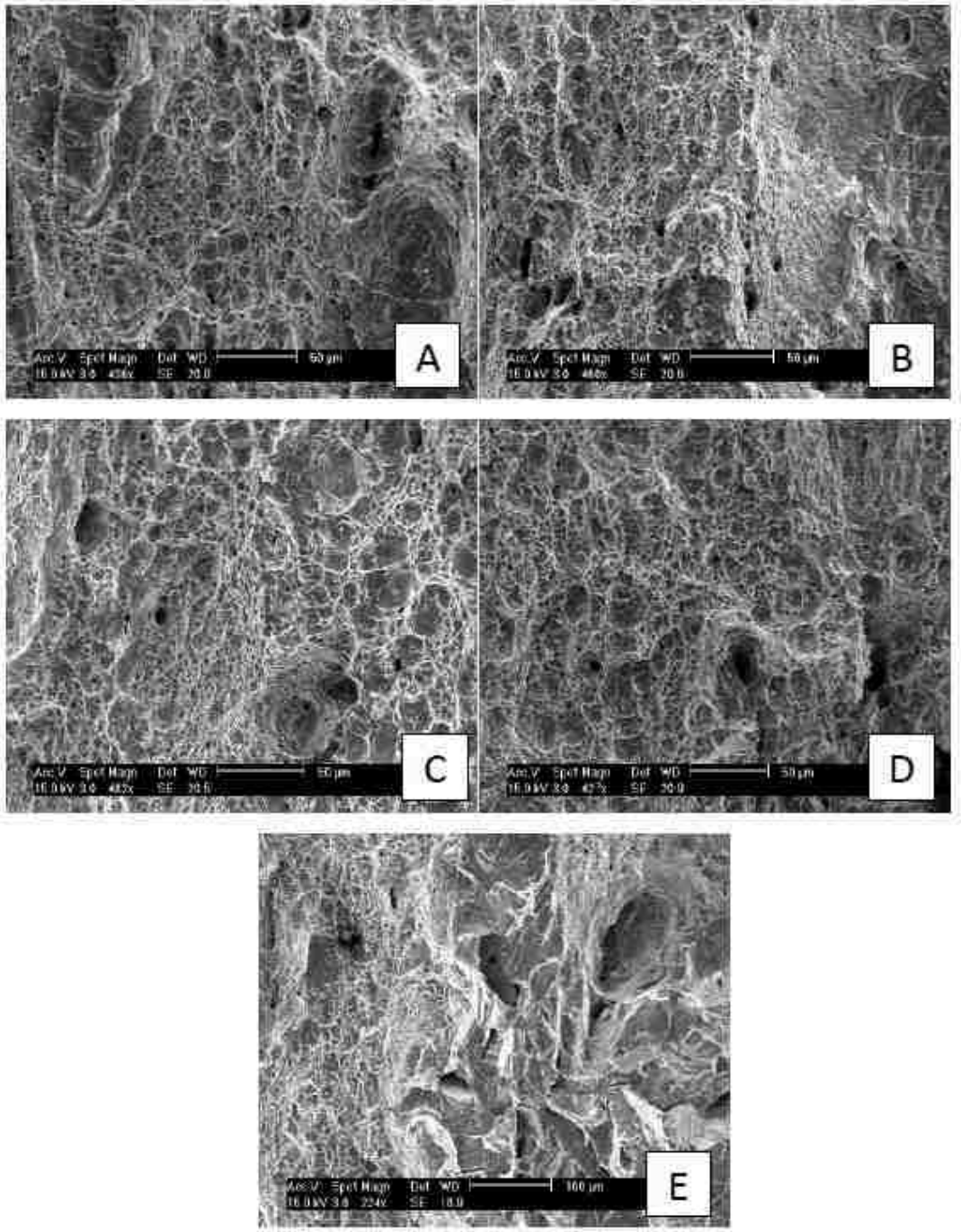

Figure 35: Fracture surfaces of NUCu-140 thermal simulations showing ductile failure via microvoid coalescence for peak temperatures of (a) base metal, (b) 675°C, (c) 800°C, and (d) 900°C. Areas of cleavage fracture are seen in (e) the 1350°C peak temperature specimen.

3.6 EDS Analysis of Particles at Microvoids

The ridges observed in the direction of primary crack growth were investigated further in order to determine the cause, specifically in the base metal sample where a larger number of smaller ridges were seen and also in the 900°C peak temperature sample where the ridges were much larger and deeper (Figure 34 (a) and (d)). Figure 36a and Figure 37a show the line of linked microvoids ahead of the ridges for the base metal and 900°C peak temperature samples, respectively. These voids were commonly observed to form by particle/matrix decohesion. Figure 36c shows an EDS spectra corresponding to a typical particle (denoted by an arrow) shown in Figure 36b for the base metal sample, and Figure 37c and Figure 37b detail the same information for the 900°C peak temperature sample. The EDS spectra show large peaks of Fe along with high Al content and smaller peaks of Ni and Cu. Further research is required in order to determine the exact nature of these particles.

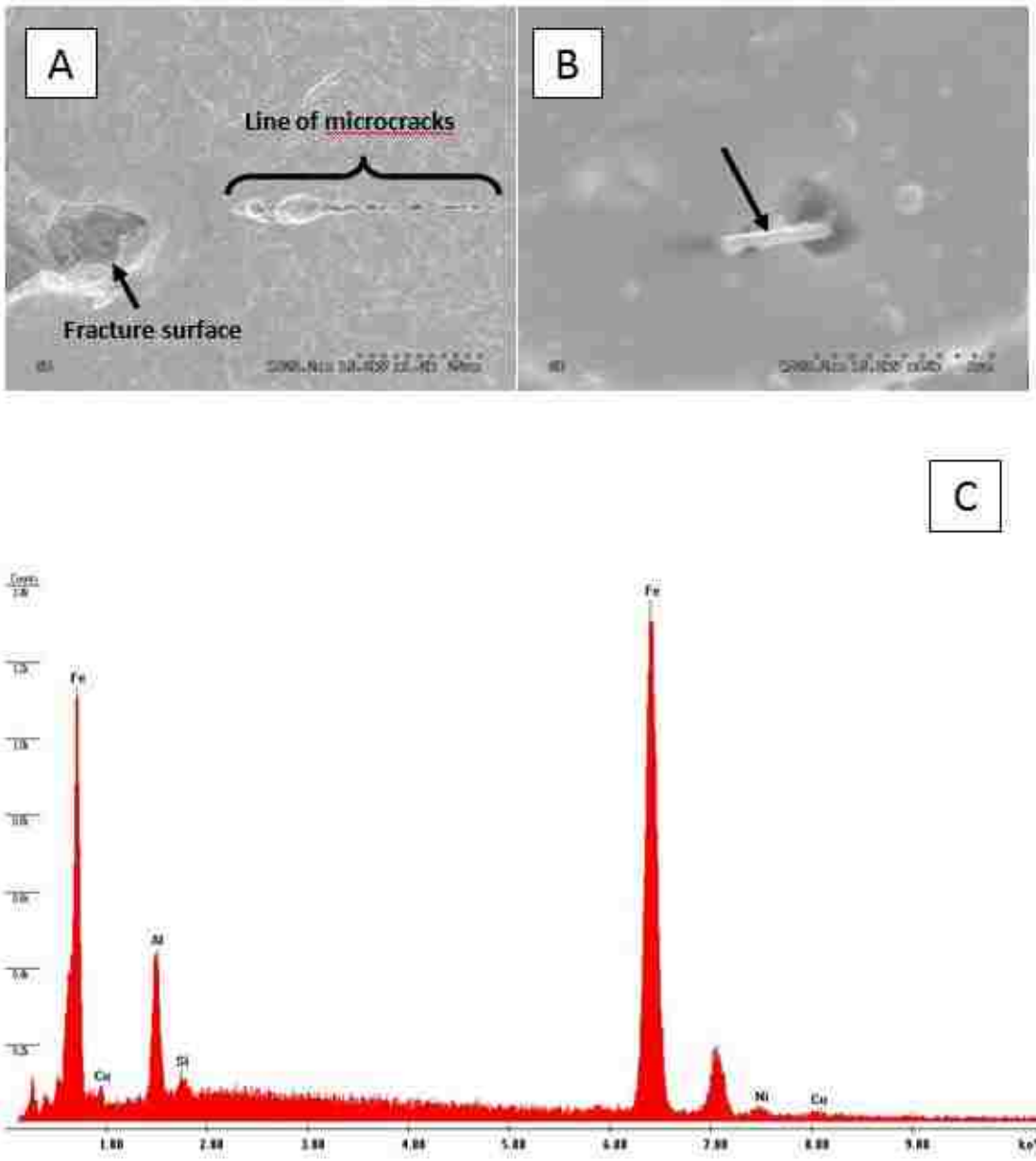

Figure 36: SEM micrographs and EDS spectra showing (a) line of microcracks ahead of a ridge in base metal sample, (b-c) particle at the edge of a microcrack shown to be an aluminum rich particle.

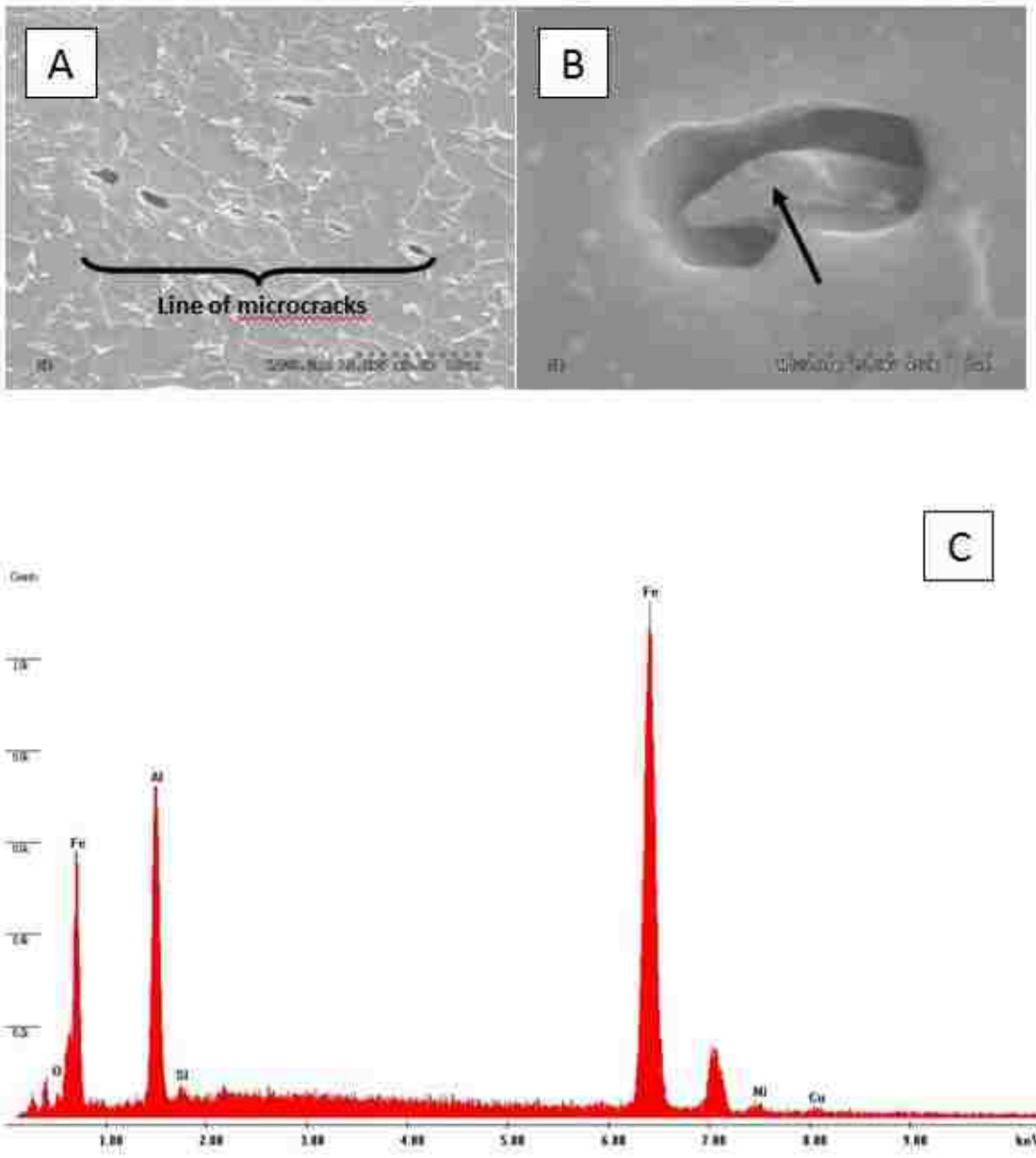

Figure 37: SEM micrographs and EDS spectra showing (a) line of microcracks ahead of a ridge in 900°C peak temperature sample, (b-c) particle at the edge of a microcrack shown to be an aluminum rich particle.

3.7 MatCalc Results

MatCalc modeling was performed in order to characterize the evolution of the precipitates in various regions of the HAZ.[1] The unaffected base metal is predicted to contain a

Cu precipitate phase fraction of 0.01. According to the modeling results, when subjected to the 675°C peak temperature, partial dissolution of the copper precipitates occurs followed by a small amount of precipitation of new smaller Cu precipitates. This leads to an overall decrease in the phase fraction to approximately 0.006. The excess copper is trapped in a solid solution with the iron matrix. The results of the 900°C and 1350°C peak temperature simulations predicts full dissolution of the copper precipitates. In comparison to the 675°C peak temperature, a higher number of new precipitates are predicted to form during the 900°C and 1350°C peak temperature thermal cycles. The final predicted phase fraction for the 900°C and 1350°C peak temperatures is approximately 0.004. The 800°C peak temperature is expected to fall in between the results for the 675°C and 900°C thermal cycles.

3.8 Discussion

Previous work by Farren et al.[1] has shown that the copper precipitates undergo considerable change in the HAZ during exposure to the weld thermal cycle. Figure 38 shows local electrode atom probe (LEAP) data for an NUCu-140 GMA weld describing the average radius, number density, and phase fraction of copper precipitates in the HAZ of NUCu-140, with HAZ 1 and HAZ 2 corresponding to the 675°C and 900°C peak temperatures, respectively. These results show that following their respective thermal cycles, the phase fraction of copper precipitates is significantly lower than the unaffected base metal. There is also an increase in number density, but a decrease in average precipitate radius for the HAZ 1 and HAZ 2 regions.

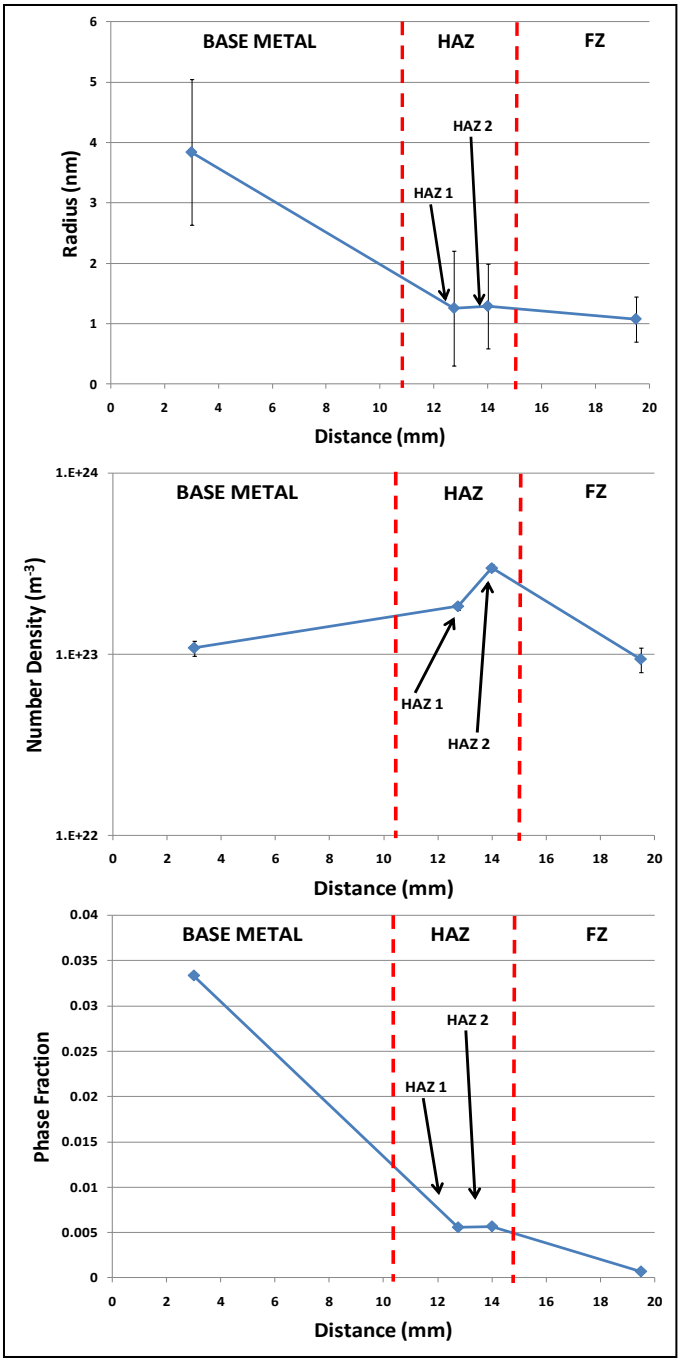

Figure 38: LEAP tomography data from NUCu-140 showing radius, number density, and phase fraction of copper precipitates in the base metal, heat affected zone, and fusion zone.[1]

The slight decrease in grain size observed in the sample exposed to a 900°C peak temperature can be attributed to grain refinement from the α → γ transformation during heating and

cooling. By heating to 900°C the material entered the fully recrystallized region where it was fully transformed to austenite, but there was not enough time at this elevated temperature to cause grain growth, resulting in a smaller grain size. The comparatively large prior austenite grain size seen in the sample heated to 1350°C is due to the material being heated well above the Ac3 temperature, and being at this elevated temperature long enough for grain growth to occur.

Although there appears to be a minor change in grain size, much of the difference in hardness and fracture toughness can be attributed to the evolution of copper precipitates in the HAZ, which can be seen in the MatCalc simulations and LEAP results. The decrease in hardness, and conversely, the increase in fracture toughness from the base metal through the 900°C peak temperature sample are due to the decrease in phase fraction of copper precipitates found within the material. It can be seen that there is an increase in fracture toughness from the 675°C peak temperature to 800°C and a further increase at 900°C, even though the phase fraction of precipitates is the same. This further increase is due to plastic deformation occurring at the crack tip in the 800°C and 900°C samples. A comparison between the 675°C and 900°C peak temperature samples is seen in Figure 39 where the 900°C sample follows the blunting line until higher crack extensions in comparison to the 675°C sample.

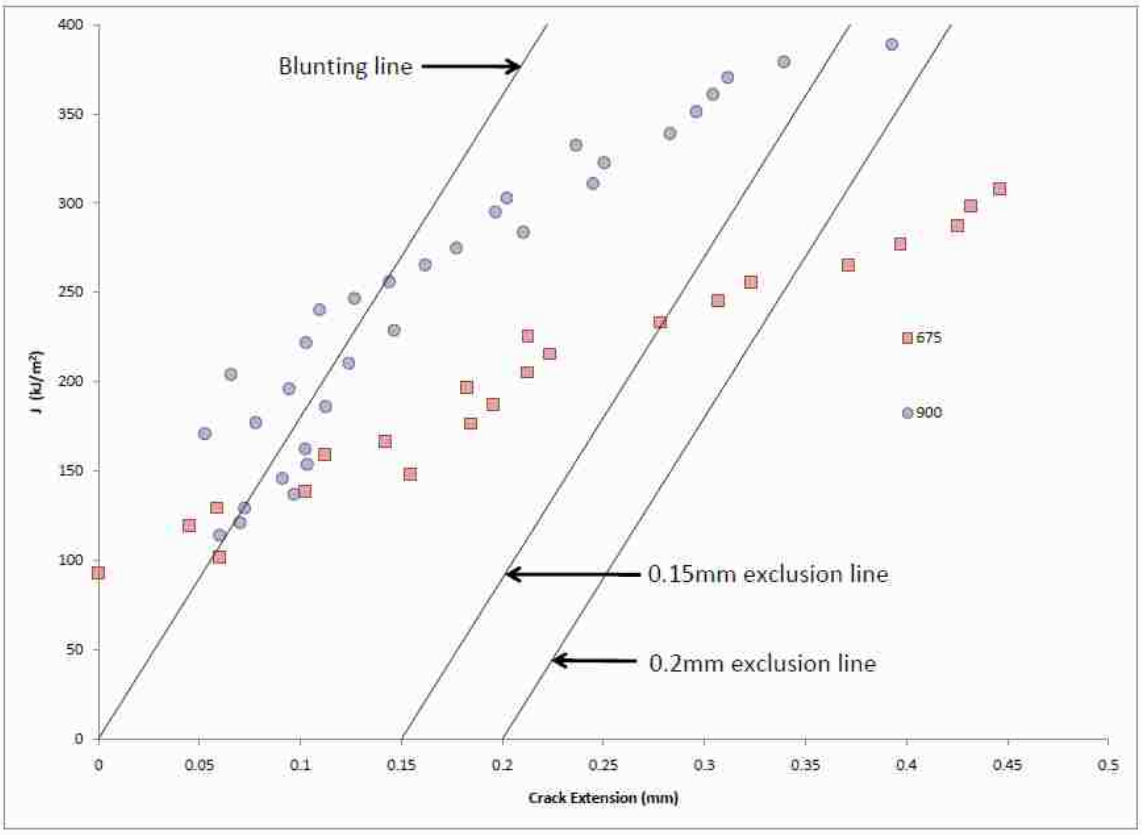

Figure 39: Close-up view of crack tip blunting region of NUCu-140 JR curves

This means that there is more energy absorbed by the 900°C sample because of the plastic deformation occurring in the form of crack tip blunting. There is a similar drop in phase fraction of copper precipitates for the 1350°C peak temperature, but its increased hardness and reduced fracture toughness is a result of the microstructure present. Although acicular ferrite, typically a tough microstructure[3], is present, there is also evidence of bainite and martensite, which results in a higher hardness but reduced fracture toughness. Further support a brittle microstructure being present in the microstructure is seen in the SEM fractographs which show regions of cleavage failure only in the 1350°C peak temperature samples.

4. Conclusions

- The reduction in hardness and the increase in fracture toughness from the base metal through the 900°C peak temperature sample are due to a decrease in the phase fraction of copper precipitates in the samples caused by coarsening and dissolution of the particles during the thermal cycles.

- Although the phase fraction of copper precipitates is the same between the 675°C, 800°C, and 900°C peak temperature samples, further increases in fracture toughness are due to increased amounts of plastic deformation are present at the crack tip because of the reduction in grain size and phase fraction of copper precipitates, which results in blunting and absorption of energy prior to crack extension.

- The increase in hardness and decrease in fracture toughness seen in the 1350°C peak temperature sample is a result of the microstructure (acicular ferrite, bainite, and martensite) that is produced from the thermal cycle.

- Microvoid coalescence is the primary failure mode for the base metal, 675°C, 800°C, and 900°C peak temperature samples, indicating ductile failure.

- Cleavage failure is seen in the 1350°C peak temperature sample indicating regions of a brittle microstructure are present, supporting observations of bainite and martensite in the microstructure.

- The fracture toughness throughout any region of the HAZ is higher than that of the unaffected base metal, meaning that the properties of the base metal can be used for design of the structure.

5. References

[1] J.D. Farren, J.N. DuPont, A.H. Hunter, D.N. Seidman, C.V. Robino, E. Kozeschnik. (Submitted May, 2011). Microstructural Evolution and Mechanical Properties of Fusion Welds in an Iron-Copper Based Multi-Component Steel. *Science and Technology of Welding and Joining* .

[2] X. Yu, J.L. Caron, S.S. Babu, J.C. Lippold, D. Isheim, D.N. Seidman. (2010). Characterization of Microstructural Strengthening in the Heat-Affected Zone of a Blast-Resistant Naval Steel. *Acta Materiala* , 5596-5609.

[3] H.K.D.H. Bhadeshia and R.W.K Honeycombe. (2006). *Steels: Microstructure and Properties.* Oxford: Elsevier

[4] J.A. Begley and J.D. Landes. (1972). The J Integral as a Fracture Criterion. In *Fracture Toughness - Proceedings of the 1971 National Symposium on Fracture Mechanics Part 2* (pp. 1-23). Philadelphia, PA: ASTM.

[5] J.W. Hutchinson. (1983). Fundamentals of the Phenomenological Theory of Nonlinear Fracture Mechanics. *Journal of Applied Mechanics* , 1042-1051.

[6] J.R. Rice. (1968). A Path Independent Integral and the Approximate Analysis of Strain Concentration by Notches and Cracks. *Journal of Applied Mechanics* , 379-386.

[7] R.W. Hertzberg. (1995). *Deformation and Fracture Mechanics and Engineering Materials.* Hoboken: John Wiley and Sons.

[8] G.A. Clarke, W.R. Andrews, P.C. Paris, and D.W. Schmidt. (1976). Single Specimen Tests for J(IC) Determination. In *Mechanics of Crack Growth - Proceedings of the Eighth National Symposium on Fracture Mechanics* (pp. 27-42). Philadelphia, PA: ASTM.

[9] J.D. Landes and J.A. Begley. (1972). The Effect of Specimen Geometry on J(IC). In *Fracture Toughness - Proceedings of the 1971 National Symposium on Fracture Mechanics Part 2* (pp. 24-39). Philadelphia, PA: ASTM.

[10] J.H. Kuang and Y.C. Chen. (1996). The Values of J-Integral Within the Plastic Zone. *Engineering Fracture Mechanics* , 869-881.

[11] S.K. Kudari, B. Maiti, K.K. Ray. (2007). The Effect of Specimen Geometry on Plastic Zone Size: A Study Using the J-Integral. *Journal of Strain Analysis* , 125-136.

[12] T.S. Koko and J.R. Matthews. (2001). Plastic Zone Development in Dynamic Tear-Type Test Specimens. *Finite Elements in Analysis and Design* , 997-1012.

[13] F.A. McClintock. (1971). Developments in Mechanics. *Proceedings of the 11th Midwestern Applied Mechanics Conference* (pp. 971-976). Ames, IA: Iowa State University Press.

[14] D.M. Kulkarni, R. Prakash, P. Talan, A.N. Kumar. (2004). The Effect of Specimen Thickness on the Experimental and Finite Element Characterization of CTOD in Extra Deep Drawn Steel Sheets. *Sadhana* , 365-380.

[15] J. Lereim and J.D. Embury. (1979). A Simple Method for the Determination of J-Integral Values. *Engineering Fracture Mechanics* , 161-164.

[16] S.K. Maiti and A.S. Keshbat. (1993). Experimental and Finite Element Study on Stable Crack Growth in Three Point Bending. *International Journal of Fracture* , 179-194.

[17] E.J. Czyryca. (1993). Advances in High Strength Steel Technology for Naval Hull Construction. *Key Engineering Materials* , 491-520.

[18] M. Ericksonkirk and M. Ericksonkirk. (2006). The Relationship Between the Transition and Upper Shelf Fracture Toughness of Ferritic Steels. *Fatigue and Fracture of Engineering Materials and Structures* , 672-684.

[19] A.K. Lis, J. Lis, L. Jeziorski. (1997). Advanced Ultra-low Carbon Bainitic Steels with High Toughness. *Journal of Materials Processing Technology* , 255-266.

[20] Y. Tomita, T. Haze, N. Saito, T. Tsuzuki, Y. Tokunaga, and K. Okamoto. (1994). Development of 590-MPa Class High Tensile Strength Steel with Superior HAZ Toughness by Copper Precipitation Hardening. *ISIJ International* , 836-842.

[21] S.K. Das, S. Sivaprasad, S. Das, S. Chatterjee, and S. Tarafder. (2006). The Effect of Variation of Microstructure on Fracture Mechanics Parameters of HSLA-100 Steel. *Materials Science and Engineering A* , 68-79.

[22] Y. Shi and Z. Han. (2008). Effect of Weld Thermal Cycle on Microstructure and Fracture Toughness of Simulated Heat-Affected Zone for a 800 MPa Grade High Strength Low Alloy Steel. *Journal of Materials Processing Technology* , 30-39.

[23] M.H. Avazkonandeh-Gharavol, M. Haddad-Sabzevar, A. Haerian. (2009). Effect of Chromium Content on the Microstructure and Mechanical Properties of Multipass MMA, Low Alloy Steel Weld Metal. *Journal of Materials Science* , 186-197.

[24] G.Z. Wang and Y. L. Wang. (2007). Effects of Loading Rate, Notch Geometry, and Loading Mode on the Local Cleavage Fracture Stress of a C-Mn Steel. *International Journal of Fracture* , 105-121.

[25] D. Chae, C.J. Young, D.M Goto, D.A. Koss. (2001). Failure Behavior of Heat-Affected Zones within HSLA-100 and HY-100 Weldments. *Metallurgical and Materials Transactions A* , 2229-2237.

[26] D. Chae, D.A. Koss, A. L. Wilson, P.R. Howell. (2000). The Effect of Microstructural Banding on Failure Initiation of HY-100 Steel. *Metallurgical and Materials Transactions A* , 995-1005.

[27] C.L. Davis and J.E. King. (1993). Effect of Cooling Rate on Intercritically Reheated Microstructure and Toughness in High Strength Low Alloy Steel. *Materials Science and Technology* , 8-15.

[28] T. Ishikawa and T. Haze. (1994). Significance of Fracture Facet Size in Cleavage Fracture Process of Welded Joints. *Materials Science and Engineering A* , 385-391.

[29] Y. Tomita. (1992). Review: Morphology Control of Ductile Second Phase and Improved Mechanical Properties in High-Strength Low-Alloy Steels with Mixed Structure. *Journal of Materials Science* , 1705-1715.

[30] Sandia National Laboratory. (2004). Software Optimizes Parameters for Automated Welding. *Advanced Materials & Processes* , 18-19.

[31] American Society for Testing and Materials. (2010). ASTM E112 - 10: Standard Test Methods for Determining Average Grain Size. In *Annual Book of ASTM Standards.*

[32] American Society for Testing and Materials. (2008). ASTM E1820 - 08: Standard Test Method for Measurement of Fracture Toughness. In *Annual Book of ASTM Standards.*

6. Vita

Brett Leister was born on April 11, 1986 in Allentown, PA to Thomas and Cheryl Leister. He grew up in Bally, PA with his parents and older brother Ryan. Brett attended The Hill School in Pottstown, PA where he excelled in science, winning the awards for highest average grade in Physics, Samuel Schaadt Prize for Excellence in Chemistry Lab, and the George C. Whiteley Jr. Prize for Excellence in All Sciences. Brett was also inducted into the Cum Laude Society. He graduated in May 2004, before attending Lehigh University in the fall. Brett was an active member on Lehigh University's Formula SAE team, while majoring in Mechanical Engineering, and double minoring in Materials Science and Engineering and History. He graduated from Lehigh in May 2008. He received his M.S. in Mechanical Engineering in May 2011, and will pursue a Ph.D. in Materials Science and Engineering.